Inorganic Chemistry

Article

pubs.acs.org/IC

Synthesis and Lewis Acid Properties of $(ReO_3F)_\infty$ and the X-ray Crystal Structures of $(HF)_2ReO_3F{\cdot}HF$ and $[N(CH_3)_4]_2[\{ReO_3(\mu\text{-}F)\}_3(\mu_3\text{-}O)]{\cdot}CH_3CN$

Maria V. Ivanova, Tobias Köchner, Hélène P. A. Mercier, and Gary J. Schrobilgen*

Department of Chemistry, McMaster University, Hamilton, Ontario L8S 4M1, Canada

Supporting Information

ABSTRACT: A high-yield, high-purity synthesis of $(ReO_3F)_\infty$ has been achieved by solvolysis of Re_2O_7 in anhydrous HF (aHF) followed by reaction of the water formed with dissolved F_2 at room temperature. The improved synthesis has allowed the Lewis acid and fluoride ion acceptor properties of $(ReO_3F)_\infty$ to be further investigated. The complex, $(HF)_2ReO_3F{\cdot}HF$, was obtained by dissolution of $(ReO_3F)_\infty$ in aHF at room temperature and was characterized by vibrational spectroscopy and single-crystal X-ray diffraction at −173 °C. The HF molecules are F-coordinated to rhenium, representing the only known example of a HF complex with rhenium. The trirhenium dianion, $[\{ReO_3(\mu\text{-}F)\}_3(\mu_3\text{-}O)]^{2-}$, was obtained as the $[N(CH_3)_4]^+$ salt by the reaction of stoichiometric amounts of $(ReO_3F)_\infty$ and $[N(CH_3)_4]F$ in CH_3CN solvent at −40 to −20 °C. The anion was structurally characterized in CH_3CN solution by ^{19}F NMR spectroscopy and in the solid state by Raman spectroscopy and a single-crystal X-ray structure determination of $[N(CH_3)_4]_2[\{ReO_3(\mu\text{-}F)\}_3(\mu_3\text{-}O)]{\cdot}CH_3CN$ at −173 °C. The structural parameters and vibrational frequencies of the $[\{MO_3(\mu\text{-}F)\}_3(\mu_3\text{-}O)]^{2-}$ and $[\{MO_3(\mu\text{-}F)\}_3(\mu_3\text{-}F)]^-$ anions (M = Re, Tc) were calculated using density functional theory. The calculated geometries of $[\{ReO_3(\mu\text{-}F)\}_3(\mu_3\text{-}O)]^{2-}$ and $[\{TcO_3(\mu\text{-}F)\}_3(\mu_3\text{-}F)]^-$, are in very good agreement with their experimental geometries. Calculated vibrational frequencies and Raman intensities have been used to assign the Raman spectra of $(HF)_2ReO_3F{\cdot}HF$ and $[N(CH_3)_4]_2[\{ReO_3(\mu\text{-}F)\}_3(\mu_3\text{-}O)]{\cdot}CH_3CN$. The X-ray crystal structures of the byproducts, $[N(CH_3)_4][ReO_4]$ and $KF{\cdot}4HF$, were also determined in the course of this work.

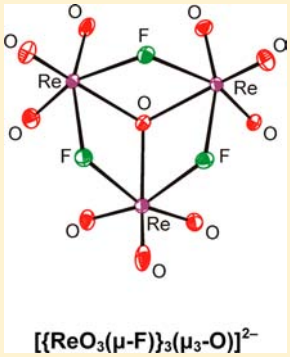

INTRODUCTION

Rhenium trioxide fluoride has been known for more than 60 years,[1] but its chemistry has been little studied. The fluoride ion acceptor properties of $(ReO_3F)_\infty$ have been investigated for several alkali metal fluorides (K,[2−4] Rb,[4] Cs[4]) and $[N(CH_3)_4]F$.[5] The resulting complexes were characterized by infrared[2−5] and Raman[3] spectroscopy and formulated as salts of the $[mer\text{-}ReO_3F_3]^{2-}$ anion,[2−5] although the isoelectronic $[OsO_3F_3]^-$ anion has since been shown to exclusively exist as the *fac*-isomer.[6] No further structural characterization of $[ReO_3F_3]^{2-}$ has been reported. More recently, the donor−acceptor complexes, $(CH_3CN)_2ReO_3F$[7] and L_2ReO_3F (L = $(C_2H_5)_2O$, $(CH_3)_2O$, THF),[8] were characterized by single-crystal X-ray diffraction, establishing the Lewis acid character of $(ReO_3F)_\infty$. Unlike the previously reported meridional geometries proposed for the $[ReO_3F_3]^{2-}$ anion, $(CH_3CN)_2ReO_3F$ and L_2ReO_3F have *cis*-trioxo arrangements. No studies of the fluoride ion donor properties of $(ReO_3F)_\infty$ have been forthcoming.

Several low-yield syntheses of $(ReO_3F)_\infty$ have been reported in the literature,[1,9−11] but none provide a reliable high-yield, high-purity synthesis of this compound, which has likely contributed to the slow development of its chemistry. For a summary of prior $(ReO_3F)_\infty$ syntheses, see ref 8. Among the synthetic routes available for $(ReO_3F)_\infty$, two are particularly relevant to the present study. The solvolyses of $K[ReO_4]$ and Re_2O_7 in aHF (eqs 1 and 2) have been documented by means of Raman and ^{19}F NMR spectroscopy; however, $(ReO_3F)_\infty$ was not isolated from these solutions.[12] The Raman assignments reported in the latter study were based on an assumed C_{3v} point symmetry for ReO_3F in aHF solution.

$$K[ReO_4] + (2 + x)HF \xrightarrow{aHF} K[F(HF)_x] + ReO_3F + H_2O \quad (1)$$

$$Re_2O_7 + 2HF \xrightarrow{aHF} 2ReO_3F + H_2O \quad (2)$$

More recently, another synthesis of $(ReO_3F)_\infty$ was reported which entailed the reaction of ReO_3 with F_2 at temperatures between 90 and 150 °C.[8] The oxidative fluorination of ReO_3 resulted in the formation of $(ReO_3F)_\infty$, which was isolated from the reaction byproducts, $ReOF_5$ and ReO_2F_3, upon condensation of $(ReO_3F)_\infty$ as a glassy sublimate in the cooler regions of the quartz reactor. The X-ray crystal structure, Raman spectrum, and mass spectrum of $(ReO_3F)_\infty$ were reported. The crystal structure was determined on a 3-fold twinned crystal and is reported to consist of a fluorine- and oxygen-bridged chain polymer having hexacoordinated rhenium atoms.

Received: October 11, 2012
Published: May 24, 2013

   dx.doi.org/10.1021/ic302221y | *Inorg. Chem.* 2013, 52, 6806−6819

Table 1. Experimental Raman Frequencies and Intensities for $(ReO_3F)_\infty$ and $(HF)_2ReO_3F{\cdot}HF$ and Calculated Vibrational Frequencies, Intensities, and Assignments for Monomeric ReO_3F

$(ReO_3F)_\infty$	$(HF)_2ReO_3F{\cdot}HF$ exptl[a,b,c,d]					monomeric ReO_3F calcd[a,e]	monomeric ReO_3F assgnts (C_{3v})[c,f]
	g	*h*	*i*	*j*	*k*		
996(100)	1017(100)	1017(100)	1017(100)	1017(100)	1009	1059(43)[16]	$\nu_s(ReO_3)$
969 sh	981(40)	981(51)	981(44)	981(49)	980	1011(10)[169]	ν_{as}(ReO3 – ReO1)
908(26) br							
813(26) br							
664(6)	669(13)	669(24)	669(16)	669(16)	666	706(3)[100]	ν(ReF)
386(21) br	400(13)	400(19)	400(15)	399(15)	403	357(4)[2]	δ(O3ReO1) – δ(O2ReO3)
354(17) br	341 sh	341(8)	341(3)	341(4)			
313(11) br	326(21)	326(28)	326(25)	326(22)	321	318(1)[12]	$\delta(ReO_3)_{umb}$
	323 sh	323 sh	323 sh	323 sh			
234(2) br	215(<1)	215(5)	215(2)	215(3)		243(2)[6]	δ(FReO2) + ρ_w(O3ReO1)
190(3) }	190(4) }	190(7) }	190(3) }	190(5) }			lattice modes
177(5) }	177(4) }	177(7) }	177(5) }	177(5) }			

[a]Frequencies are given in cm^{-1}. [b]Values in parentheses denote relative Raman intensities. [c]The abbreviations denote shoulder (sh), broad (br), stretch (ν), bend (δ), symmetric (s), asymmetric (as), wag (ρ_w), and umbrella (umb). [d]Raman spectra were recorded in FEP sample tubes at −150 °C using 1064-nm excitation. [e]Values in parentheses denote calculated Raman intensities ($Å^4\ u^{-1}$). Values in square brackets denote calculated infrared intensities (km mol^{-1}). The B3LYP/aug-cc-pVTZ(-PP) method was used. [f]The atom numbering corresponds to that used in Figure S1 where O1, O2, and O3 correspond to the three equivalent oxygen atoms of the O_3Re group. [g]From $[NH_4][ReO_4]$ dissolved in HF. [h]From $K[ReO_4]$ dissolved in HF. [i]From Re_2O_7 dissolved in HF. [j]From $(ReO_3F)_\infty$ dissolved in HF. [k]From a HF solution of Re_2O_7; ref 12.

The present paper describes a simplified and reliable synthesis of $(ReO_3F)_\infty$ and extends the Lewis acid and fluoride ion acceptor properties of $(ReO_3F)_\infty$ by the structural characterization of $(HF)_2ReO_3F{\cdot}HF$ and the cage anion, $[\{ReO_3(\mu\text{-}F)\}_3(\mu_3\text{-}O)]^{2-}$, which represent the only example of rhenium coordinated to HF and the only example of rhenium oxide fluoride species containing a tricoordinated oxygen atom.

RESULTS AND DISCUSSION

Syntheses of $(ReO_3F)_\infty$, $(HF)_2ReO_3F{\cdot}HF$, and $[N(CH_3)_4]_2[\{ReO_3(\mu\text{-}F)\}_3(\mu_3\text{-}O)]$. Reaction progress and product purities were routinely monitored by recording the Raman spectra of the solids at −150 °C.

(a) $(ReO_3F)_\infty$. The synthesis of $(ReO_3F)_\infty$ was achieved by solvolysis of Re_2O_7 in aHF followed by room-temperature fluorination of this solution with F_2 gas to oxidatively fluorinate H_2O to O_2 and HF (eqs 2 and 3). Hydrogen fluoride solvent and associated HF in the complex, $(HF)_2ReO_3F{\cdot}HF$ (vide infra), were removed under dynamic vacuum in stages at temperatures ranging from −78 °C to room temperature.

$$H_2O + F_2 \xrightarrow{aHF} 2HF + {}^1/_2O_2 \qquad (3)$$

The product was further pumped on at 50 °C to ensure complete removal of coordinated HF. Rhenium trioxide fluoride was obtained as a pale yellow, friable powder that gave a broad Raman spectrum (Figure S1, Supporting Information) identical to the previously reported spectrum.[8]

(b) $(HF)_2ReO_3F{\cdot}HF$. The complex, $(HF)_2ReO_3F{\cdot}HF$, was synthesized by dissolution of $(ReO_3F)_\infty$ in aHF (eq 4) and was isolated as pale yellow to colorless plates upon removal of

$${}^1/_\infty(ReO_3F)_\infty + 3HF \xrightarrow{aHF} (HF)_2ReO_3F{\cdot}HF \qquad (4)$$

aHF under vacuum at −78 °C. The product was characterized by single-crystal X-ray diffraction and Raman spectroscopy. The Raman spectrum of the crystalline material (Table 1) was in good agreement with the reported solution spectra resulting from the solvolyses of Re_2O_7 or $K[ReO_4]$ in aHF solvent, which have been previously assigned to monomeric ReO_3F.[12] The $(HF)_2ReO_3F{\cdot}HF$ complex was also synthesized by the solvolyses of $M[ReO_4]$ ($M = [NH_4]^+, K^+$) and Re_2O_7 in aHF (eqs 1 and 2) and was confirmed from the Raman spectra of the products, which crystallized from aHF at −78 °C, and by unit cell determinations of the single crystals.

(c) $[N(CH_3)_4]_2[\{ReO_3(\mu\text{-}F)\}_3(\mu_3\text{-}O)]$. The salt, $[N(CH_3)_4]_2[\{ReO_3(\mu\text{-}F)\}_3(\mu_3\text{-}O)]$, was obtained, along with minor amounts of $[N(CH_3)_4][ReO_4]$ and $[N(CH_3)_4][ReO_2F_4]$, by the reaction of stoichiometric quantities of $(ReO_3F)_\infty$ and $[N(CH_3)_4]F$ in CH_3CN. The product mixture was partially soluble in CH_3CN at −10 °C. Upon slow warming of the mixture to room temperature, all products dissolved forming a bright yellow solution. The salt, $[N(CH_3)_4]_2[\{ReO_3(\mu\text{-}F)\}_3(\mu_3\text{-}O)]$, was obtained in admixture with $[N(CH_3)_4][ReO_4]$ and $[N(CH_3)_4][ReO_2F_4]$ upon removal of CH_3CN at −40 to −35 °C. Subsequent drying of the mixture at room temperature yielded a friable light beige powder. The reaction of ca. 50 mg of $(ReO_3F)_\infty$ and $[N(CH_3)_4]F$ in 0.2−0.3 mL of CH_3CN led to the formation of $[N(CH_3)_4]_2[\{ReO_3(\mu\text{-}F)\}_3(\mu_3\text{-}O)]$ as the major product, whereas larger amounts (80−100 mg) of $(ReO_3F)_\infty$ and $[N(CH_3)_4]F$ in 0.3−0.4 mL of CH_3CN favored the formation of $[N(CH_3)_4][ReO_4]$ and $[N(CH_3)_4][ReO_2F_4]$. All products were characterized by single-crystal X-ray diffraction and Raman spectroscopy. Fluorine-19 NMR spectroscopy was also employed to obtain the spectra of $[N(CH_3)_4]_2[\{ReO_3(\mu\text{-}F)\}_3(\mu_3\text{-}O)]$ and $[N(CH_3)_4][ReO_2F_4]$ (see NMR Spectroscopy).

A plausible reaction pathway leading to $[\{ReO_3(\mu\text{-}F)\}_3(\mu_3\text{-}O)]^{2-}$ is given in Scheme 1. The proposed reaction sequence is initiated by dissolution of $(ReO_3F)_\infty$ in CH_3CN at −40 °C to give $(CH_3CN)_2ReO_3F$. The latter coordination complex was previously formed by the hydrolysis of ReO_2F_3 in CH_3CN solution and characterized by single-crystal X-ray diffraction.[7] In the present work, it was shown by Raman spectroscopy and single-crystal X-ray diffraction that $(ReO_3F)_\infty$ dissolves in CH_3CN to give $(CH_3CN)_2ReO_3F$ (eq 5).

$${}^1/_\infty(ReO_3F)_\infty + 2CH_3CN \xrightarrow[-40\,^\circ C]{CH_3CN} (CH_3CN)_2ReO_3F \qquad (5)$$

A second reaction, also initiated at −40 °C, leads to disproportionation of $(ReO_3F)_\infty$ in the presence of F^- ion and the formation of equimolar amounts of $[N(CH_3)_4][ReO_4]$

dx.doi.org/10.1021/ic302221y | Inorg. Chem. 2013, 52, 6806−6819

Scheme 1. Proposed Reaction Pathway Leading to the Formation of the $[\{ReO_3(\mu\text{-}F)\}_3(\mu_3\text{-}O)]^{2-}$ Anion[a]

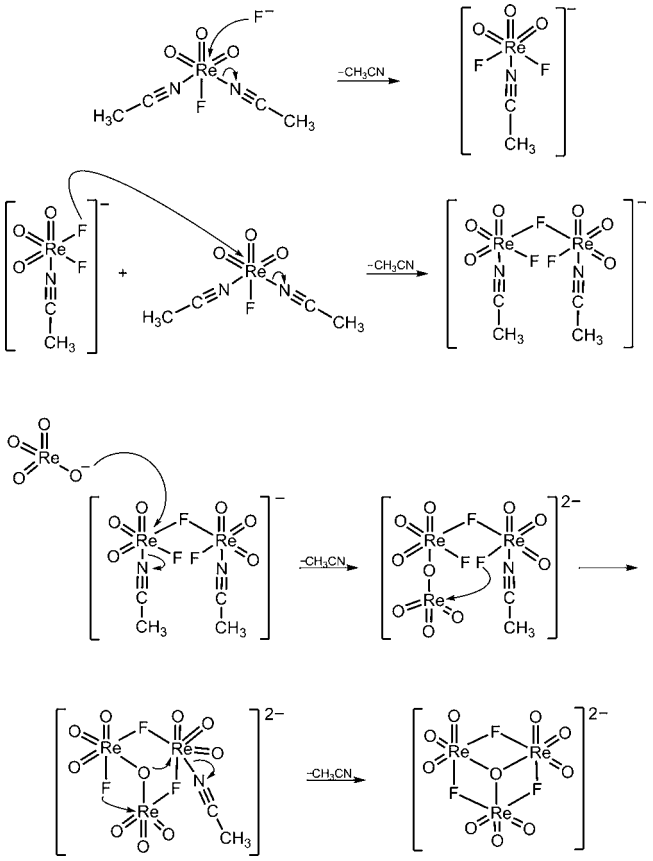

[a]The $[ReO_4]^-$ is formed in eq 6.

and $[N(CH_3)_4][ReO_2F_4]$ (eq 6) as confirmed by the Raman spectrum of the product mixture under CH_3CN at −150 °C.

$$(ReO_3F)_\infty + [N(CH_3)_4]F \xrightarrow[-40\,^\circ C]{CH_3CN} [N(CH_3)_4][ReO_4] + [N(CH_3)_4][ReO_2F_4] \quad (6)$$

A third reaction (Scheme 1), presumably involves F^- ion attack at rhenium in $(CH_3CN)_2ReO_3F$, resulting in the formation of $[(CH_3CN)ReO_3F_2]^-$ as an intermediate. The $[(CH_3CN)ReO_3F_2]^-$ anion subsequently reacts with a second equivalent of $(CH_3CN)_2ReO_3F$ to form the anionic intermediate, $[\{(CH_3CN)ReO_3F\}_2(\mu\text{-}F)]^-$. The $[ReO_4]^-$ anion functions as a nucleophile, attacking $[\{(CH_3CN)ReO_3F\}_2(\mu\text{-}F)]^-$ at rhenium to form the open chain trirhenium intermediate, $[(ReO_3)(\mu\text{-}O)(ReO_3F)(\mu\text{-}F)\{(CH_3CN)ReO_3F\}]^{2-}$, which undergoes cyclolization to $[\{ReO_3(\mu\text{-}F)\}_3(\mu_3\text{-}O)]^{2-}$. A likely alternative reaction pathway that initially involves nucleophilic attack by F^- and $[ReO_4]^-$ on two independent $(CH_3CN)_2ReO_3F$ molecules and pursuant condensation and cyclolization reactions that lead to the $[\{ReO_3(\mu\text{-}F)\}_3(\mu_3\text{-}O)]^{2-}$ anion is outlined in Scheme S1 of the Supporting Information.

In view of the existence of the $[\{TcO_3(\mu\text{-}F)\}_3(\mu_3\text{-}F)]^-$ anion,[13] attempts were made to synthesize the rhenium analogue, $[\{ReO_3(\mu\text{-}F)\}_3(\mu_3\text{-}F)]^-$. Initially, $(ReO_3F)_\infty$ was allowed to react with $[N(CH_3)_4]F$ in CH_3CN in a 3:1 molar ratio between −40 and −35 °C. The only products observed by Raman spectroscopy and single-crystal X-ray diffraction were the known $[N(CH_3)_4][ReO_4]$ salt[14] and $(CH_3CN)_2ReO_3F$.[7] A second attempt involved a reaction analogous to that used to synthesize the $[\{TcO_3(\mu\text{-}F)\}_3(\mu_3\text{-}F)]^-$ anion in aHF[13] (see Scheme S2 in the Supporting Information for a plausible reaction pathway). Thus, $K[ReO_4]$ or $[NH_4][ReO_4]$ were allowed to react with aHF at room temperature. Upon removal of aHF under dynamic vacuum, mixtures of $K/[NH_4][ReO_4]$, $(K/[NH_4][ReO_3F_2])_\infty$, $K/[NH_4][ReO_2F_4]$, and $K[H_3O]$-$[ReO_3F_3]$ were recovered as the only reaction products. The product identities were confirmed by the Raman spectra of the mixtures and by the single-crystal X-ray structures of these salts. The structures of the $(K/[NH_4][ReO_3F_2])_\infty$ and $K[H_3O]$-$[ReO_3F_3]$ salts will be discussed in a subsequent publication.

A major difference between the two reaction pathways (Schemes 1 and S2 in the Supporting Information) lies in the nature of the reaction media. In the basic solvent, CH_3CN, the $[ReO_4]^-$ anion serves as a source of the tricoordinate oxygen bridge in its reaction with the intermediate anion, $[\{(CH_3CN)ReO_3F\}_2(\mu\text{-}F)]^-$, whereas in acidic (aHF) solution, the $[MO_4]^-$ (M = Tc, Re) anion immediately undergoes HF solvolysis to form MO_3F and $[H_3O]^+$.[12,15]

NMR Spectroscopy. The ^{19}F NMR spectrum (Figure 1) of a solution resulting from the reaction of $[N(CH_3)_4]F$ and

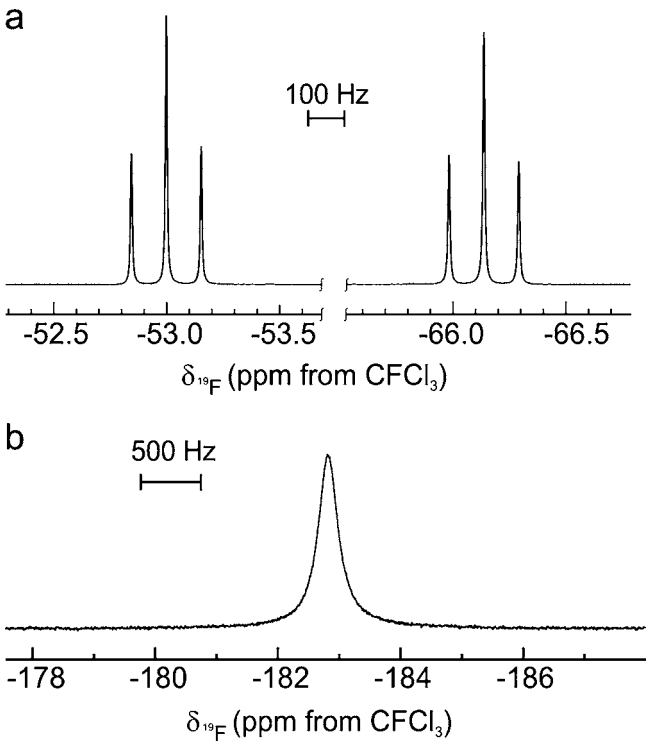

Figure 1. The ^{19}F NMR spectra (470.599 MHz) of the (a) $[ReO_2F_4]^-$ and (b) $[\{ReO_3(\mu\text{-}F)\}_3(\mu_3\text{-}O)]^{2-}$ anions in $[N(CH_3)_4][ReO_2F_4]$ and $[N(CH_3)_4]_2[\{ReO_3(\mu\text{-}F)\}_3(\mu_3\text{-}O)]$, respectively, recorded at 27 °C in CH_3CN.

$(ReO_3F)_\infty$ (1:1 stoichiometry) was recorded in CH_3CN at 27 °C and consisted of a broad signal ($\delta(^{19}F)$ = −182.8 ppm, $\nu_{1/2}$ = 213 Hz) and two sharp ($\nu_{1/2}$ = 5.0 Hz), equal-intensity triplets ($\delta(^{19}F)$ = −53.0 ppm ($F_{c,t}$); $\delta(^{19}F)$ = −66.1 ppm ($F_{c,c}$) and $^2J(^{19}F_{c,t}-^{19}F_{c,c})$ = 87 Hz, where the c and t subscripts denote cis and trans to oxygen, respectively) that are unambiguously assigned to [*cis*-$ReO_2F_4]^-$, in agreement with the published ^{19}F NMR spectrum.[7] The broad singlet at −182.8 ppm is tentatively assigned to a fluorine bridge environment by

dx.doi.org/10.1021/ic302221y | Inorg. Chem. 2013, 52, 6806−6819

comparison with the bridging fluorine resonance of $[(ReO_2F_3)_2(\mu\text{-}F)]^-$ (−141.2 ppm).[7] The ^{19}F NOE and $^{19}F-^{19}F$ COSY spectra did not show any NOE or correlation between the two triplets of $[cis\text{-}ReO_2F_4]^-$ and the broad singlet, thus confirming their independence and the presence of a single fluorine environment in the unknown species. The NMR findings are in accordance with the X-ray crystal structure of $[\{ReO_3(\mu\text{-}F)\}_3(\mu_3\text{-}O)]^{2-}$ (Structure I), which contains three equivalent bridging fluorine atoms (see X-ray Crystallography) and which was also observed, along with $[ReO_4]^-$, in the room-temperature Raman spectrum of the reaction mixture dissolved in CH_3CN.

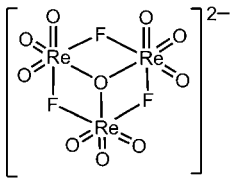

I

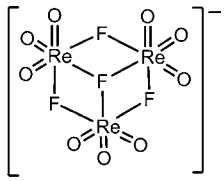

II

To further investigate the nature of the species associated with the ^{19}F resonance at −182.8 ppm, the ^{19}F NMR chemical shift of $[\{ReO_3(\mu\text{-}F)\}_3(\mu_3\text{-}O)]^{2-}$ was calculated at the PBE0/SO/ZORA/TZ2P level. The chemical shift obtained was referenced to the chemical shift of the bridging fluorine of the structurally related $[(ReO_2F_3)_2(\mu\text{-}F)]^-$ anion of its $[N(CH_3)_4]^+$ salt in CH_3CN solvent at −40 °C (−141.2 ppm with respect to $CFCl_3$; also see Experimental and Computational Results).[7] The calculated ^{19}F chemical shift of the three equivalent bridging F_μ atoms of $[\{ReO_3(\mu\text{-}F)\}_3(\mu_3\text{-}O)]^{2-}$ is −179.3 ppm, in very good agreement with the experimental value, −182.8 ppm.

For comparison, the isotropic ^{19}F chemical shifts of the three bridging F_μ atoms (−203.9 ppm) and the central three-coordinate bridging $F_{\mu 3}$ atom (−195.9 ppm) in the related $[\{ReO_3(\mu\text{-}F)\}_3(\mu_3\text{-}F)]^-$ anion (Structure II) were also calculated. Taking into account the estimated error in the calculated chemical shift (±20 ppm),[16,17] the observed broad resonance at −182.8 ppm, in principle, could also be assigned to the $[\{ReO_3(\mu\text{-}F)\}_3(\mu_3\text{-}F)]^-$ anion, with the broadening of the resonance arising from intramolecular fluorine chemical exchange between the F_μ and $F_{\mu 3}$ environments of $[\{ReO_3(\mu\text{-}F)\}_3(\mu_3\text{-}F)]^-$. Unfortunately, variable temperature experiments, which may have led to splitting or further coalescence of the resonance, could not be performed because crystalline material deposited at 0 °C and slow decomposition took place above ca. 40 °C.

On the basis of ^{19}F NMR chemical shifts alone, it is not possible to unambiguously determine the solution structure of the anion, nor is it possible to differentiate between $[\{ReO_3(\mu\text{-}F)\}_3(\mu_3\text{-}O)]^{2-}$ and $[\{ReO_3(\mu\text{-}F)\}_3(\mu_3\text{-}F)]^-$; however, from Raman spectroscopic findings, the X-ray crystal structure, and synthetic considerations (see Synthesis of $[N(CH_3)_4]_2[\{ReO_3(\mu\text{-}F)\}_3(\mu_3\text{-}O)]$), it is reasonable to conclude that the $[\{ReO_3(\mu\text{-}F)\}_3(\mu_3\text{-}O)]^{2-}$ anion retains its solid-state structure in solution.

X-ray Crystallography. Details of the data collection and other crystallographic information for $(HF)_2ReO_3F\cdot HF$, $[N(CH_3)_4]_2[\{ReO_3(\mu\text{-}F)\}_3(\mu_3\text{-}O)]\cdot CH_3CN$, $[N(CH_3)_4][ReO_4]$, and KF·4HF are given in Table 2, and important bond lengths and bond angles for $(HF)_2ReO_3F\cdot HF$ and $[\{ReO_3(\mu\text{-}F)\}_3(\mu_3\text{-}O)]^{2-}$ are provided in Tables 3 and 4. The crystal structure of KF·4HF is given in Figure S2 (Supporting Information).

The crystal structure of $[N(CH_3)_4]_2[\{ReO_3(\mu\text{-}F)\}_3(\mu_3\text{-}O)]\cdot CH_3CN$ consists of well-separated $[N(CH_3)_4]^+$ cations, $[\{ReO_3(\mu\text{-}F)\}_3(\mu_3\text{-}O)]^{2-}$ anions, and CH_3CN molecules (Figure S3, Supporting Information), and the crystal structure of $[N(CH_3)_4][ReO_4]$ consists of well-separated $[N(CH_3)_4]^+$ cations and $[ReO_4]^-$ anions (Figure S4, Supporting Information). In both structures, the tetrahedral $[N(CH_3)_4]^+$ cations lie on C_3-axes. The N−C bond lengths are equal within experimental error and are comparable to those given in the literature.[6,18,19] The geometrical parameters of the CH_3CN molecule are also in good agreement with the literature values.[7,20]

(a) $[N(CH_3)_4][ReO_4]$. The $[ReO_4]^-$ anion has T_d symmetry with a Re−O bond length (1.726(3) Å) that is in good agreement with the Re−O bond lengths of other $[ReO_4]^-$ salts (K^+, 1.719(5) Å, at 20 °C;[21] $[NH_4]^+$, 1.737(5) Å, at −138 °C and 1.720(5) Å, at 22 °C[22]).

(b) $(HF)_2ReO_3F\cdot HF$. The crystal structure of $(HF)_2ReO_3F\cdot HF$ reveals that the coordination sphere of rhenium is a distorted octahedron consisting of three oxygen atoms that are cis to one another, a fluorine atom, and two HF

Table 2. Summary of Crystal Data and Refinement Results for $[N(CH_3)_4]_2[\{ReO_3(\mu\text{-}F)\}_3(\mu_3\text{-}O)]\cdot CH_3CN$, $[N(CH_3)_4][ReO_4]$, $(HF)_2ReO_3F\cdot HF$, and KF·4HF

chem formula	$[N(CH_3)_4]_2[\{ReO_3(\mu\text{-}F)\}_3(\mu_3\text{-}O)]\cdot CH_3CN$	$[N(CH_3)_4][ReO_4]$	$(HF)_2ReO_3F\cdot HF$	KF·4HF
space group	$P2_1/c$	$Pbcm$	$P2_1/c$	$I4_1/a$
a (Å)	9.1792(5)	5.7222(3)	4.9381(3)	6.287(5)
b (Å)	20.3457(12)	11.8535(5)	4.9392(3)	6.287(5)
c (Å)	14.3432(6)	12.4754(6)	20.716(1)	12.937(5)
β (deg)	124.3(3)	90	91.906(2)	90
V (Å)^3	2212.8(2)	845.57(7)	505.02(8)	511.4(1)
molecules/unit cell	4	4	4	4
mol wt (g mol^{-1})	964.95	1297.38	1252.90	536.40
calcd density (g cm^{-3})	2.896	2.548	4.120	1.742
T (°C)	−173	−173	−173	−173
μ (mm^{-1})	16.44	14.33	24.08	1.02
R_1[a]	0.0371	0.0338	0.0371	0.0299
wR_2[b]	0.0782	0.0841	0.0931	0.0838

[a] R_1 is defined as $\Sigma||F_o| - |F_c||\Sigma|F_o|$ for $I > 2\sigma(I)$. [b] wR_2 is defined as $[\Sigma[w(F_o^2 - F_c^2)^2]/\Sigma w(F_o^2)^2]^{1/2}$ for $I > 2\sigma(I)$.

dx.doi.org/10.1021/ic302221y | Inorg. Chem. 2013, 52, 6806−6819

Table 3. Experimental Bond Lengths (Å) and Bond Angles (deg) for $(HF)_2ReO_3F{\cdot}HF$ and Calculated Bond Lengths (Å) and Bond Angles (deg) for Monomeric ReO_3F

exptl[a]		calcd[b]	
$(HF)_2ReO_3F{\cdot}HF$		ReO_3F (C_{3v})	
Bond Lengths (Å)			
Re(1)−O(1)	1.669(5)	Re−O1	1.693
Re(1)−O(2)	1.662(5)	Re−O2	1.693
Re(1)−O/F(3)	1.838(5)	Re−O3	1.693
Re(1)−O/F(4)	1.837(4)	Re−F	1.844
Re(1)---F(1)	2.045(4)		
Re(1)---F(2)	2.014(4)		
Bond Angles (deg)			
O(1)−Re(1)−O(2)	102.9(3)	O1−Re−O2	109.0
O(1)−Re(1)−O(3)	95.9(3)	O1−Re−O3	109.0
O(2)−Re(1)−O(3)	96.7(3)	O2−Re−O3	109.0
O(3)−Re(1)−F(4)	159.1(3)	O3−Re−F	109.9
O(1)−Re(1)−F(4)	97.1(3)	O1−Re−F	109.9
O(2)−Re(1)−F(4)	96.5(3)	O2−Re−F	109.9
F(1)---Re(1)---F(2)	75.2(2)		
F(4)−Re(1)---F(2)	81.7(2)		
O(3)−Re(1)---F(2)	81.8(2)		
O(2)−Re(1)---F(1)	166.9(2)		
O(2)−Re(1)---F(2)	91.7(2)		
O(1)−Re(1)---F(1)	90.0(2)		
O(1)−Re(1)---F(2)	165.3(2)		
O(3)−Re(1)---F(1)	82.1(2)		
F(1)---Re(1)−F(4)	81.3(2)		

[a]The labeling scheme corresponds to that used in Figure 2. [b]B3LYP/aug-cc-pVTZ(-PP). The labeling scheme corresponds to that used in Figure S1.

molecules that are cis to one another and trans to oxygen ligands (Figure 2). The HF molecules are coordinated to the rhenium atom through their F atoms, representing the only known example of HF coordinated to rhenium. Several examples in which HF is coordinated to alkaline earth and lanthanide metal cations[23] and to Os(VIII)[24] are also known. The facial arrangement of oxygen atoms is the result of equal competition of the filled p orbitals of the oxygen atoms for the three empty approximately $d_{t_{2g}}$ orbitals of rhenium.[25] The rhenium atom is found to lie in the [F(1), F(2), O(1), O(2)] plane and is equidistant from the disordered F/O(3, 4) atoms. The Re−O(1, 2) bond lengths trans to the two HF molecules (1.669(5) and 1.662(5) Å) are very similar to the Re−O bond lengths in polymeric $(ReO_2F_3)_\infty$ (1.667(8) and 1.675(8) Å)[7] and (1.669(9)−1.676(9) Å),[8] but are somewhat shorter than those of $(CH_3CN)_2ReO_3F$ (1.705(4) and 1.788(5) Å)[7] and $(OEt_2)_2ReO_3F$ (1.703(3), 1.708(3), and 1.778(2) Å).[8] The third Re−O bond length could not be accurately determined due to a 2-fold positional disorder between O/F(3) and F/O(4). These bond lengths (1.838(5) and 1.837(4) Å) are the average of the Re−O (1.788(5) Å) and Re−F (1.880(5) Å)[7] bond lengths of $(CH_3CN)_2ReO_3F$.[7] The Re---F(1, 2) distances (2.045(4) and 2.014(4) Å) are comparable to the Re---F bridging distances in oligomeric $(ReO_2F_3)_\infty$ (2.085(6)−2.118(7) Å)[7] (2.075(7)−2.109(6) Å)[8] and $(ReO_3F)_\infty$ (2.141(7)−2.142(7) Å).[8] The O/F(3)−Re−F/O(4) bond angle (159.1(3)°) is bent away from the Re−O(1, 2) double bond domain toward the less repulsive Re---F(1, 2) bonds. The O(1)−Re−O(2) angle (102.9(3)°) is considerably more open than the F(1)---Re---F(2) angle (75.2(2)°) as a result of greater repulsions between the Re−O(1) and Re−O(2) double bond domains, with weaker repulsions occurring between the longer and more polar Re---F(1, 2) bond domains. In turn, the small F(1)---Re---F(2) angle is a consequence of repulsive interactions between the Re---F(1, 2) bond domains and the Re−O(1, 2) double bond domains.

(c) $[N(CH_3)_4]_2[\{ReO_3(\mu\text{-}F)\}_3(\mu_3\text{-}O)]{\cdot}CH_3CN$. The $[\{ReO_3(\mu\text{-}F)\}_3(\mu_3\text{-}O)]^{2-}$ anion is positioned on a C_3-axis and consists of three ReO_3F units linked to each other through dicoordinate bridging fluorine atoms (F_μ) and a central tricoordinate bridging oxygen atom ($O_{\mu 3}$). The bridge-head $O_{\mu 3}$ atom is located on the C_3-axis, and the coordination environments of the rhenium atoms are pseudo-octahedral (Figure 3).

A closely related structure with a triply coordinated oxygen bridge atom has been reported for the $[\{WF_3(\mu\text{-}O)\}_3(\mu_3\text{-}O)]^{5-}$ anion in $[NH_4]_5[\{WF_3(\mu\text{-}O)\}_3(\mu_3\text{-}O)]{\cdot}[NH_4]F{\cdot}H_2O$.[26] The Re atoms of $[\{ReO_3(\mu\text{-}F)\}_3(\mu_3\text{-}O)]^{2-}$ form a triangle with Re···Re distances of 3.4128(3) Å (Re(1)···Re(2)), 3.3910(4) Å (Re(2)···Re(3)), and 3.3870(3) Å (Re(3)···Re(1)). The Re···Re distances are significantly longer than the W···W distances (2.514(2) Å) of the W_3-triangle in $[\{WF_3(\mu\text{-}O)\}_3(\mu_3\text{-}O)]^{5-}$,[26] which is indicative of significant W−W bonding. Rhenium in $[\{ReO_3(\mu\text{-}F)\}_3(\mu_3\text{-}O)]^{2-}$ is in the +7 oxidation state (Re, $5d^0$), where the terminal coordination sites are occupied by doubly bonded oxygen ligands and the μ-bridge positions are occupied by bridging fluorine ligands. In contrast, tungsten in $[\{WF_3(\mu\text{-}O)\}_3(\mu_3\text{-}O)]^{5-}$ is in the +4 oxidation state (W, $5d^2$) where the terminal coordination sites are occupied by fluorine ligands and the μ-bridge positions are occupied by oxygen ligands. The influence of $O_{\mu 3}$ on both structures is minor. The structural parameters are dominated by the metal oxidation state. Thus, the availability of the d^2 valence electrons of $[\{WF_3(\mu\text{-}O)\}_3(\mu_3\text{-}O)]^{5-}$ allows metal−metal bond formation among the tungsten metal centers, resulting in W···W distances that are substantially shorter than the Re···Re distances in $[\{ReO_3(\mu\text{-}F)\}_3(\mu_3\text{-}O)]^{2-}$. Presently, neither tungsten oxide fluorides in higher oxidation states nor rhenium oxide fluorides in lower oxidation states having similar structural motifs, which could substantiate the observed trend, are known. However, several examples of similar trends occur among rhenium and tungsten chlorides and chloro-anions. Rhenium(III) trichloride exists as a Re_3Cl_9 cluster with Re···Re distances of 2.489(6) Å,[27] whereas Re(V)Cl_5 contains Re_2Cl_{10} units with a substantially longer Re···Re distance of 3.739(2) Å.[28] In comparison, the W···W distances are 2.409(5) Å in $K_3[W_2(III)Cl_9]$,[29] and 2.8703(6)−2.9054(6) Å in the octahedral W_6-cluster of $K_2[W_6(III)Cl_{18}]$.[30]

The central bridging $O_{\mu 3}$ and bridging F_μ atoms of $[\{ReO_3(\mu\text{-}F)\}_3(\mu_3\text{-}O)]^{2-}$ coordinate trans to the terminal oxygen atoms (O_t) of the facial ReO_3 group so that the filled oxygen p orbitals of the O_t atoms compete equally for the three empty $d_{t_{2g}}$ orbitals of rhenium.[25] The Re(1), Re(2), and Re(3) atoms lie in the [F(1), F(2), O(1), O(3)], [F(2), F(3), O(4), O(6)], and [F(3), F(1), O(7), O(9)] planes, respectively. The Re−O_t bonds are comparable in length to those in oligomeric $(ReO_3F)_\infty$ (1.667(7)−1.715(8) Å),[8] $(ReO_2F_3)_\infty$ (1.667(8)−1.675(8) Å)[7] and (1.669(9)−1.676(9) Å),[8] $[ReO_4]^-$ (1.726(3) Å, this work), $[ReO_2F_4]^-$ (1.678(9) Å),[7] and $[(ReO_2F_2)(\mu\text{-}F)_2(ReO_2F_3)_2]^-$ (1.669(8)−1.715(8) Å).[7] The bridging Re−F_μ bond lengths are comparable to the Re−F_μ bond lengths in $(ReO_3F)_\infty$ (2.141(7) and 2.142(7) Å),[8] $(ReO_2F_3)_\infty$

dx.doi.org/10.1021/ic302221y | Inorg. Chem. 2013, 52, 6806−6819

Table 4. Experimental Structural Parameters for the $[\{ReO_3(\mu\text{-}F)\}_3(\mu_3\text{-}O)]^{2-}$ Anion in $[N(CH_3)_4]_2[\{ReO_3(\mu\text{-}F)\}_3(\mu_3\text{-}O)]\cdot CH_3CN$ and Calculated Structural Parameters for the $[\{ReO_3(\mu\text{-}F)\}_3(\mu_3\text{-}O)]^{2-}$ and $[\{ReO_3(\mu\text{-}F)\}_3(\mu_3\text{-}F)]^{-}$ Anions

exptl[a]		calcd[b,c]			
$[\{ReO_3(\mu\text{-}F)\}_3(\mu_3\text{-}O)]^{2-}$		$[\{ReO_3(\mu\text{-}F)\}_3(\mu_3\text{-}O)]^{2-}$		$[\{ReO_3(\mu\text{-}F)\}_3(\mu_3\text{-}F)]^{-}$	
		Bond Lengths (Å)			
Re(1)−O(1)	1.711(4)	Re_1-O_A	1.707	Re_1-O_A	1.695
Re(1)−O(2)	1.706(4)	Re_1-O_B	1.714	Re_1-O_B	1.696
Re(1)−O(3)	1.713(4)	Re_1-O_C	1.707	Re_1-O_C	1.695
Re(2)−O(4)	1.705(4)	Re_2-O_A	1.707	Re_2-O_A	1.695
Re(2)−O(5)	1.716(4)	Re_2-O_B	1.714	Re_2-O_B	1.696
Re(2)−O(6)	1.705(4)	Re_2-O_C	1.707	Re_2-O_C	1.695
Re(3)−O(7)	1.703(4)	Re_3-O_A	1.707	Re_3-O_A	1.695
Re(3)−O(8)	1.666(5)	Re_3-O_B	1.714	Re_3-O_B	1.696
Re(3)−O(9)	1.700(4)	Re_3-O_C	1.707	Re_3-O_C	1.695
Re(1)−O(10)	2.079(4)	Re_1-O_D	2.106	Re_1-F_4	2.319
Re(2)−O(10)	2.072(4)	Re_2-O_D	2.106	Re_2-F_4	2.319
Re(3)−O(10)	2.078(4)	Re_3-O_D	2.106	Re_3-F_4	2.319
Re(1)−F(1)	2.139(3)	Re_1-F_1	2.165	Re_1-F_1	2.123
Re(1)−F(2)	2.166(3)	Re_1-F_2	2.165	Re_1-F_2	2.123
Re(2)−F(2)	2.163(3)	Re_2-F_2	2.165	Re_2-F_2	2.123
Re(2)−F(3)	2.148(3)	Re_2-F_3	2.165	Re_2-F_3	2.123
Re(3)−F(3)	2.144(3)	Re_3-F_3	2.165	Re_3-F_3	2.123
Re(3)−F(1)	2.140(3)	Re_3-F_1	2.165	Re_3-F_1	2.123
		Bond Angles (deg)			
O(1)−Re(1)−O2	102.6(2)	$O_A-Re_1-O_B$	104.3	$O_A-Re_1-O_B$	105.2
O(2)−Re(1)−O(3)	105.4(2)	$O_B-Re_1-O_C$	104.3	$O_B-Re_1-O_C$	105.2
O(3)−Re(1)−O(1)	104.0(2)	$O_C-Re_1-O_A$	102.2	$O_C-Re_1-O_A$	103.2
O(1)−Re(1)−O(10)	95.4(2)	$O_A-Re_1-O_D$	95.9	$O_A-Re_1-F_4$	90.0
O(2)−Re(1)−O(10)	148.2(2)	$O_B-Re_1-O_D$	147.4	$O_B-Re_1-F_4$	155.1
O(3)−Re(1)−O(10)	94.4(2)	$O_C-Re_1-O_D$	95.9	$O_C-Re_1-F_4$	90.0
O(4)−Re(2)−O(5)	104.2(2)	$O_A-Re_2-O_B$	104.3	$O_A-Re_2-O_B$	105.2
O(5)−Re(2)−O(6)	105.1(2)	$O_B-Re_2-O_C$	104.3	$O_B-Re_2-O_C$	105.2
O(6)−Re(2)−O(4)	102.7(2)	$O_C-Re_2-O_A$	102.2	$O_C-Re_2-O_A$	103.2
O(4)−Re(2)−O(10)	94.4(2)	$O_A-Re_2-O_D$	95.9	$O_A-Re_2-F_4$	90.0
O(5)−Re(2)−O(10)	148.4(2)	$O_B-Re_2-O_D$	147.4	$O_B-Re_2-F_4$	155.1
O(6)−Re(2)−O(10)	95.2(2)	$O_C-Re_2-O_D$	95.9	$O_C-Re_2-F_4$	90.0
O(7)−Re(3)−O(8)	104.6(2)	$O_A-Re_3-O_B$	104.3	$O_A-Re_3-O_B$	105.2
O(8)−Re(3)−O(9)	105.2(2)	$O_B-Re_3-O_C$	104.3	$O_B-Re_3-O_C$	105.2
O(9)−Re(3)−O(7)	103.2(2)	$O_C-Re_3-O_A$	102.2	$O_C-Re_3-O_A$	103.2
O(7)−Re(3)−O(10)	94.9(2)	$O_A-Re_3-O_D$	95.9	$O_A-Re_3-F_4$	90.0
O(8)−Re(3)−O(10)	147.5(2)	$O_B-Re_3-O_D$	147.4	$O_B-Re_3-F_4$	155.1
O(9)−Re(3)−O(10)	95.1(2)	$O_C-Re_3-O_D$	95.9	$O_C-Re_3-F_4$	90.0
O(1)−Re(1)−F(2)	87.3(2)	$O_A-Re_1-F_2$	88.3	$O_A-Re_1-F_2$	87.9
O(2)−Re(1)−F(2)	86.0(2)	$O_B-Re_1-F_2$	85.9	$O_B-Re_1-F_2$	93.6
O(3)−Re(1)−F(2)	162.3(2)	$O_C-Re_1-F_2$	162.8	$O_C-Re_1-F_2$	154.6
O(10)−Re(1)−F(2)	69.9(1)	$O_D-Re_1-F_2$	69.3	$F_4-Re_1-F_2$	66.9
O(1)−Re(1)−F(1)	162.2(2)	$O_A-Re_1-F_1$	162.8	$O_A-Re_1-F_1$	154.6
O(2)−Re(1)−F(1)	84.6(2)	$O_B-Re_1-F_1$	85.9	$O_B-Re_1-F_1$	93.6
O(3)−Re(1)−F(1)	89.7(2)	$O_C-Re_1-F_1$	88.3	$O_C-Re_1-F_1$	87.9
O(10)−Re(1)−F(1)	69.9(1)	$O_D-Re_1-F_1$	69.3	$F_4-Re_1-F_1$	66.9
O(4)−Re(2)−F(2)	88.9(2)	$O_A-Re_2-F_2$	88.3	$O_A-Re_2-F_2$	87.9
O(5)−Re(2)−F(2)	84.8(2)	$O_B-Re_2-F_2$	85.9	$O_B-Re_2-F_2$	93.6
O(6)−Re(2)−F(2)	162.1(2)	$O_C-Re_2-F_2$	162.8	$O_C-Re_2-F_2$	154.6
O(10)−Re(2)−F(2)	70.0(1)	$O_D-Re_2-F_2$	69.3	$F_4-Re_2-F_2$	66.9
O(4)−Re(2)−F(3)	161.9(2)	$O_A-Re_2-F_3$	162.8	$O_A-Re_2-F_3$	154.6
O(5)−Re(2)−F(3)	86.2(2)	$O_B-Re_2-F_3$	85.9	$O_B-Re_2-F_3$	93.6
O(6)−Re(2)−F(3)	88.6(2)	$O_C-Re_2-F_3$	88.3	$O_C-Re_2-F_3$	87.9
O(10)−Re(2)−F(3)	70.2(1)	$O_D-Re_2-F_3$	69.3	$F_4-Re_2-F_3$	66.9
O(7)−Re(3)−F(3)	162.3(2)	$O_A-Re_3-F_3$	162.8	$O_A-Re_3-F_3$	154.6
O(8)−Re(3)−F(3)	85.2(2)	$O_B-Re_3-F_3$	85.9	$O_B-Re_3-F_3$	93.6
O(9)−Re(3)−F(3)	87.9(2)	$O_C-Re_3-F_3$	88.3	$O_C-Re_3-F_3$	87.9

dx.doi.org/10.1021/ic302221y | Inorg. Chem. 2013, 52, 6806−6819

Table 4. continued

exptl[a]		calcd[b,c]			
$[\{ReO_3(\mu\text{-}F)\}_3(\mu_3\text{-}O)]^{2-}$		$[\{ReO_3(\mu\text{-}F)\}_3(\mu_3\text{-}O)]^{2-}$		$[\{ReO_3(\mu\text{-}F)\}_3(\mu_3\text{-}F)]^{-}$	
		Bond Angles (deg)			
O(10)−Re(3)−F(3)	70.2(1)	O_D−Re_3−F_3	69.3	F_4−Re_3−F_3	66.9
O(7)−Re(3)−F(1)	88.2(2)	O_A−Re_3−F_1	88.3	O_A−Re_3−F_1	87.9
O(8)−Re(3)−F(1)	84.3(2)	O_B−Re_3−F_1	85.9	O_B−Re_3−F_1	93.6
O(9)−Re(3)−F(1)	162.5(2)	O_C−Re_3−F_1	162.8	O_C−Re_3−F_1	154.6
O(10)−Re(3)−F(1)	70.4(1)	O_D−Re_3−F_1	69.3	F_4−Re_3−F_1	66.9
F(1)−Re(1)−F(2)	77.7(1)	F_1−Re_1−F_2	78.5	F_1−Re_1−F_2	73.7
F(2)−Re(2)−F(3)	77.1(1)	F_2−Re_2−F_3	78.5	F_2−Re_2−F_3	73.7
F(3)−Re(3)−F(1)	78.1(1)	F_3−Re_3−F_1	78.5	F_3−Re_3−F_1	73.7
Re(1)−O(10)−Re(2)	110.6(2)	Re_1−O_D−Re_2	110.2	Re_1−F_4−Re_2	103.9
Re(2)−O(10)−Re(3)	109.6(2)	Re_2−O_D−Re_3	110.2	Re_2−F_4−Re_3	103.9
Re(3)−O(10)−Re(1)	109.1(2)	Re_3−O_D−Re_1	110.2	Re_3−F_4−Re_1	103.9
Re(1)−F(2)−Re(2)	104.1(1)	Re_1−F_2−Re_2	105.9	Re_1−F_2−Re_2	118.7
Re(2)−F(3)−Re(3)	104.4(1)	Re_2−F_3−Re_3	105.9	Re_2−F_3−Re_3	118.7
Re(3)−F(1)−Re(1)	104.4(1)	Re_3−F_1−Re_1	105.9	Re_3−F_1−Re_1	118.7

[a]For the atom labeling scheme, see Figure 3. [b]For the atom labeling scheme, see Figure 6. [c]B3LYP/aug-cc-pVTZ(-PP).

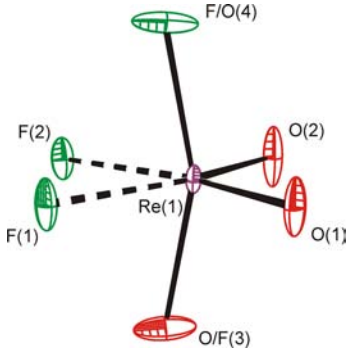

Figure 2. Structural unit in the X-ray crystal structure of $(HF)_2ReO_3F{\cdot}HF$ with thermal ellipsoids drawn at the 30% probability level. The F/O(4) and O/F(3) positions are 2-fold disordered.

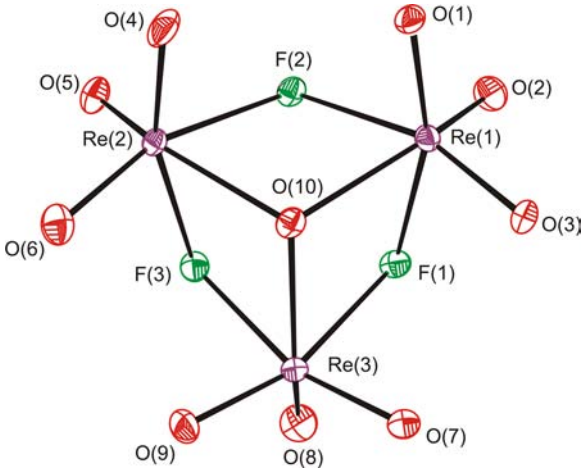

Figure 3. $[\{ReO_3(\mu\text{-}F)\}_3(\mu_3\text{-}O)]^{2-}$ anion in the crystal structure of $[N(CH_3)_4]_2[\{ReO_3(\mu\text{-}F)\}_3(\mu_3\text{-}O)]{\cdot}CH_3CN$. Thermal ellipsoids are shown at the 50% probability level.

(2.085(6)−2.118(7) Å,[7] 2.075(7)−2.109(6) Å[8]), $[(ReO_2F_3)_2(\mu\text{-}F)]^-$ (2.155(4)−2.150(4) Å),[7] and $[(ReO_2F_2)(\mu\text{-}F)_2(ReO_2F_3)_2]^-$ (2.039(6)−2.151(6) Å).[7]

A tricoordinate bridge-head oxygen atom, $O_{\mu3}$, has not been previously observed in a rhenium oxide fluoride structure. The rhenium atoms of $[\{ReO_3(\mu\text{-}F)\}_3(\mu_3\text{-}O)]^{2-}$ are equidistant (within $\pm3\sigma$) from $O_{\mu3}$ (2.072(4)−2.079(4) Å). These Re−$O_{\mu3}$ bonds are comparable in length to the Re−O_μ bonds of Re_2O_7 (2.05(2)−2.16(3) Å),[31] and to the Re−$O_{\mu3}$ bonds of $[NEt_4]_2[\{Re(CO)_3(\mu\text{-}H)\}_3(\mu_3\text{-}O)]$ (2.12 Å),[32] and $\{(t\text{-}Bu)_2SiO_2\}_2(\mu\text{-}O)_4(\mu_3\text{-}O)_2\{ReO(NAr)\}_2\{Re(NAr)\}_2$ (Ar = 2,6-^{i}Pr$_2$−C_6H_3; 2.170(5) Å).[33] The Re−$O_{\mu3}$ bridge bonds of $[\{ReO_3(\mu\text{-}F)\}_3(\mu_3\text{-}O)]^{2-}$ are longer than the terminal Re−O_t bonds and slightly shorter than the Re−F_μ bonds of this anion. These bond length trends differ from those of the related $[\{TcO_3(\mu\text{-}F)\}_3(\mu_3\text{-}F)]^-$ anion where the Tc−$F_{\mu3}$ bonds (2.223(3)−2.266(3) Å) are longer than the Tc−F_μ bonds (2.098(3)−2.132(3) Å).[13] The experimental bond length trends for $[\{ReO_3(\mu\text{-}F)\}_3(\mu_3\text{-}O)]^{2-}$ and $[\{TcO_3(\mu\text{-}F)\}_3(\mu_3\text{-}F)]^-$ are reproduced by quantum-chemical calculations (see Computational Results).

The O_t−Re−O_t angles of $[\{ReO_3(\mu\text{-}F)\}_3(\mu_3\text{-}O)]^{2-}$ are greater than the O_t−Re−F_μ and F_μ−Re−F_μ angles due to the greater spatial requirements of the terminal oxygen double bond domains which result in greater repulsive interactions with other bond pair domains as observed in $[ReO_2F_4]^-$,[7] $[(ReO_2F_3)_2(\mu\text{-}F)]^-$,[7] $[(ReO_2F_2)(\mu\text{-}F)_2(ReO_2F_3)_2]^-$,[7] $(ReO_2F_3)_\infty$,[7,8] and $(ReO_3F)_\infty$.[8] Compression of the F_μ−Re−F_μ angles of $[\{ReO_3(\mu\text{-}F)\}_3(\mu_3\text{-}O)]^{2-}$ relative to the F_μ−Re−F_μ (70.4(1)−77.7(1)°) angles of $[(ReO_2F_3)_2(\mu\text{-}F)]^-$, $[(ReO_2F_2)(\mu\text{-}F)_2(ReO_2F_3)_2]^-$, and $(ReO_2F_3)_\infty$ is also attributable to the greater spatial requirements of the Re−O_t double bond domains and to constraints imposed by the anion cage. The latter factor also influences the $O_{\mu3}$−Re−F_μ angles, which are the smallest of the anion cage angles (69.3°). The largest cage angles occur for the Re−$O_{\mu3}$−Re angles (109.1(2)−110.6(2)°), which are more open than the angles subtended at $O_{\mu3}$ in $\{(t\text{-}Bu)_2SiO_2\}_2(\mu\text{-}O)_4(\mu_3\text{-}O)_2\{ReO(NAr)\}_2\{Re(NAr)\}_2$ (104.8(2)°).[33]

Raman Spectroscopy. The low-temperature Raman spectra of $(HF)_2ReO_3F{\cdot}HF$ and $[N(CH_3)_4]_2[\{ReO_3(\mu\text{-}F)\}_3(\mu_3\text{-}O)]{\cdot}CH_3CN$ are shown in Figures 4 and 5. The observed and calculated frequencies and mode descriptions for $(HF)_2ReO_3F{\cdot}HF$, $[ReO_4]^-$, and $[\{ReO_3(\mu\text{-}F)\}_3(\mu_3\text{-}O)]^{2-}$ are provided in Tables 1, S1, and 5, respectively. Spectral assignments for the $[N(CH_3)_4]^+$ cation[34−36] and CH_3CN[20] were made by comparison with previously published

dx.doi.org/10.1021/ic302221y | Inorg. Chem. 2013, 52, 6806−6819

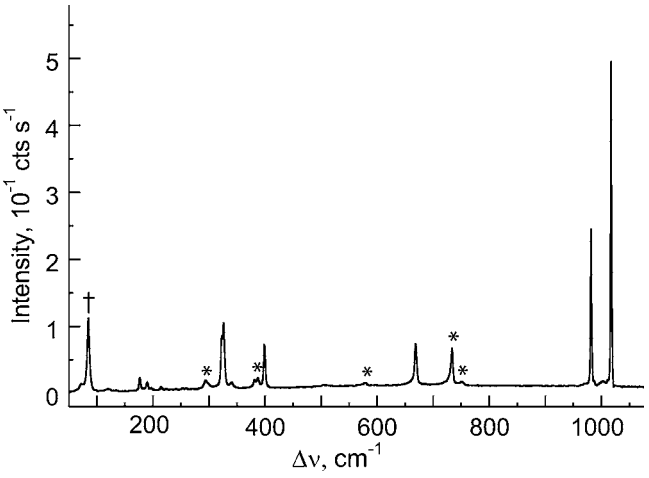

Figure 4. Raman spectrum of $(HF)_2ReO_3F{\cdot}HF$ obtained from the solvolysis of $(ReO_3F)_\infty$ in aHF and isolated by removal of aHF under dynamic vacuum at −78 °C. The spectrum is recorded at −160 °C using 1064-nm excitation. Symbols denote FEP sample tube lines (*) and an instrumental artifact (†).

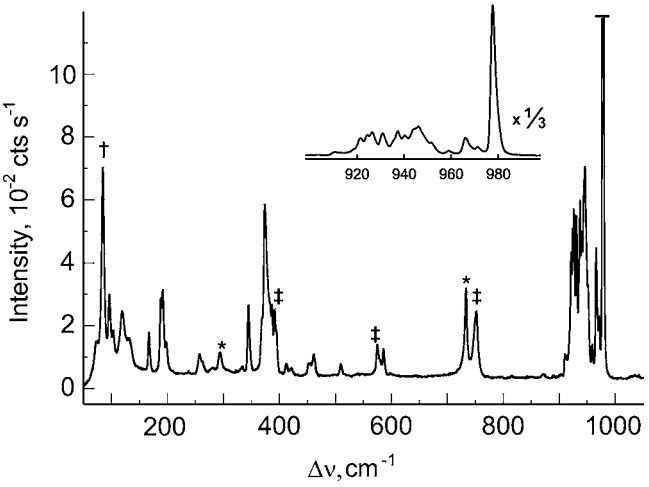

Figure 5. Raman spectrum of $[N(CH_3)_4]_2[\{ReO_3(\mu\text{-}F)\}_3(\mu_3\text{-}O)]{\cdot}CH_3CN$ recorded under frozen CH_3CN at −150 °C using 1064-nm excitation. Symbols denote FEP sample tube lines (*), instrumental artifact (†), and overlap of a $[N(CH_3)_4]_2[\{ReO_3(\mu\text{-}F)\}_3(\mu_3\text{-}O)]{\cdot}CH_3CN$ line with a FEP sample tube line (‡).

assignments. Spectral assignments for $[\{ReO_3(\mu\text{-}F)\}_3(\mu_3\text{-}O)]^{2-}$ were made by comparison with the calculated frequencies and Raman intensities of the energy-minimized gas-phase geometries of $[ReO_4]^-$ (T_d) and $[\{ReO_3(\mu\text{-}F)\}_3(\mu_3\text{-}O)]^{2-}$ (C_{3v}), where gas-phase $[ReO_4]^-$ was used as a benchmark. The vibrational assignments for $[ReO_4]^-$ are provided in Table S2 and in the ensuing discussion provided in the Supporting Information, and agree with the previously published assignments.[37,38]

(a) $(HF)_2ReO_3F{\cdot}HF$. The Raman spectrum of solid $(HF)_2ReO_3F{\cdot}HF$ is similar to those reported for solutions of Re_2O_7 and $K[ReO_4]$ in aHF.[12] The present study, however, establishes that the previously reported solution spectra correspond to a $ReO_3F{\cdot}n$HF complex and not to ReO_3F (C_{3v}), as proposed by the authors.[12] In the present study, the spectrum is simpler than that of $(ReO_3F)_\infty$,[8] lacking modes in the Re−O−Re and Re−F−Re bridging stretching regions.

The $(HF)_2ReO_3F$ complex has 21 fundamental vibrational modes under C_{2v} symmetry belonging to the irreducible representations $8A_1 + 4B_1 + 3A_2 + 6B_2$, where all modes are Raman active and the A_1, B_1, and B_2 modes are infrared active. The four anions occupy C_1 sites in the crystallographic unit cell of $(HF)_2ReO_3F{\cdot}HF$. A factor-group analysis was carried out (Table S2, Supporting Information) based on the crystal structure (see X-ray crystal structure of $(HF)_2ReO_3F{\cdot}HF$). Correlation of the gas-phase symmetry of the complex (C_{2v}) to the crystal site symmetry (C_1) results in no additional splittings for the A_1, B_1, A_2, and B_2 modes. Correlation of the site symmetry to the crystal (unit cell) symmetry (C_{2h}) shows that the A_1, B_1, A_2, and B_2 modes are split into Raman-active A_g and B_g components and into infrared-active A_u and B_u components. Only 10 of the 21 Raman-active vibrational modes predicted for $(HF)_2ReO_3F$ in the gas phase were observed. Modes associated with the coordinated HF molecules are expected to be weak and were not observed in the Raman spectrum. Vibrational coupling within the unit cell of $(HF)_2ReO_3F{\cdot}HF$ is apparently weak, and, consequently, the splittings are too small to be resolved on many of the bands.

The bands at 981 and 1017 cm^{-1} are assigned to the asymmetric and symmetric Re−O stretching modes, respectively, and appear at higher frequencies than in $(ReO_3F)_\infty$ (969−996 cm^{-1}). The intense band at 669 cm^{-1} is in good agreement with the 664 cm^{-1} band observed in $(ReO_3F)_\infty$ and is assigned to an Re−F stretching mode. The bands between 215 and 399 cm^{-1} are assigned to O−Re−O and F−Re−O deformation modes which are similar to those observed in $(ReO_3F)_\infty$ (234−386 cm^{-1}).

(b) $[N(CH_3)_4]_2[\{ReO_3(\mu\text{-}F)\}_3(\mu_3\text{-}O)]{\cdot}CH_3CN$. The anion, $[\{ReO_3(\mu\text{-}F)\}_3(\mu_3\text{-}O)]^{2-}$, possesses 42 fundamental vibrational modes belonging to the irreducible representations $9A_1 + 5A_2 + 14E$ under C_{3v} symmetry, where the A_1 and E modes are Raman and infrared active and the A_2 modes are inactive. The four anions occupy C_1 sites in the crystallographic unit cell of $[N(CH_3)_4]_2[\{ReO_3(\mu\text{-}F)\}_3(\mu_3\text{-}O)]{\cdot}CH_3CN$. As a result of site symmetry lowering, all E modes are expected to be split into two A components. In order to assign the additional bands that could not be accounted for by symmetry lowering alone, the possibility of vibrational coupling within the unit cell was investigated by undertaking a factor-group analysis (Table S3, Supporting Information) based on the crystal structure of $[N(CH_3)_4]_2[\{ReO_3(\mu\text{-}F)\}_3(\mu_3\text{-}O)]{\cdot}CH_3CN$. Although correlation of the gas-phase anion symmetry (C_{3v}) to its crystal site symmetry (C_1) cannot result in splittings for the A_1 and A_2 modes, correlation of the site symmetry to the unit cell symmetry (C_{2h}) showed that the A_1 and A_2 modes are each split into Raman-active A_g and B_g components and into infrared-active A_u and B_u components under C_{2h} crystal symmetry. Each E mode is split into two A_g and two B_g components that are Raman-active and two A_u and two B_u components that are infrared-active. The factor-group splittings predicted for the Raman spectrum were observed on the highest intensity bands, namely, $\nu_1(A_1)$ (971/978), $\nu_{10}(E)$ (946/951/959/966), $\nu_{11}(E)$ (931/937/941/944), $\nu_2(A_1)$ (924/926), $\nu_4(A_1)$ (392/395), $\nu_8(A_1)$ (191/197), $\nu_{12}(E)$ (911/918/921), and $\nu_{13}(E)$ (575/580/586).

The bands between 911 and 978 cm^{-1} are assigned to the out-of-phase and in-phase terminal Re−O stretching modes. The two factor-group split bands at highest frequency (971, 978 cm^{-1}) correspond to the totally symmetric $\nu_{in\text{-}phase}$(Re−O) stretching mode. The calculated frequencies reproduce the

dx.doi.org/10.1021/ic302221y | Inorg. Chem. 2013, 52, 6806−6819

Table 5. Experimental Raman Frequencies and Intensities for the $[\{ReO_3(\mu\text{-}F)\}_3(\mu_3\text{-}O)]^{2-}$ Anion in $[N(CH_3)_4]_2[\{ReO_3(\mu\text{-}F)\}_3(\mu_3\text{-}O)]\cdot CH_3CN$ and Calculated Vibrational Frequencies and Infrared and Raman Intensities for the $[\{ReO_3(\mu\text{-}F)\}_3(\mu_3\text{-}O)]^{2-}$ and $[\{ReO_3(\mu\text{-}F)\}_3(\mu_3\text{-}F)]^{-}$ Anions

$[\{ReO_3(\mu\text{-}F)\}_3(\mu_3\text{-}O)]^{2-}$			assgnts $(C_{3v})^{c,h}$	$[\{ReO_3(\mu\text{-}F)\}_3(\mu_3\text{-}F)]^{-}$	
exptl[a,b,c]	calcd[a,d]			calcd[a,d]	
978(100) 971(6)	1018(171)[44]	$\nu_1(A_1)$	$\nu(Re_1O_AO_BO_C) + \nu(Re_2O_AO_BO_C) + \nu(Re_3O_AO_BO_C)$	$\nu_1(A_1)$	1048(155)[11]
966(13)[e] 959(4) 951(9)[f] 946(20)	1005(3)[133]	$\nu_{10}(E)$	$\nu(Re_1O_AO_BO_C) - \nu(Re_2O_AO_BO_C) + \nu(Re_3O_AO_BO_C)$	$\nu_{10}(E)$	1041(1)[72]
944 sh 941(14) 937(17) 931(16)	967(35)[270]	$\nu_{11}(E)$	$\nu(Re_1O_A) - \nu(Re_1O_C) - \nu(Re_2O_A) + \nu(Re_2O_C)$	$\nu_{11}(E)$	999(28)[225]
926(16)[e] 924(15)	959(14)[558]	$\nu_2(A_1)$	$\nu(Re_1O_B) + \nu(Re_2O_B) + \nu(Re_3O_B)$	$\nu_2(A_1)$	997(6)[459]
921(12)[g] 918 sh[g] 911(3) br	942(36)[92]	$\nu_{12}(E)$	$\nu(Re_1O_B) - \nu(Re_2O_B) + \nu(Re_2O_A) + \nu(Re_2O_C) + \nu(Re_3O_B) - \nu(Re_3O_C)$	$\nu_{12}(E)$	985(20)[73]
586(3) 580 sh 575(3)	558(6)[215]	$\nu_{13}(E)$	$[\nu(Re_2O_D) - \nu(Re_3O_D)] + [\nu(Re_1F_1) + \nu(Re_3F_1) - \nu(Re_1F_2) - \nu(Re_2F_2)]$		
			$[\nu(Re_2F_4) - \nu(Re_3F_4)] + [\nu(Re_1F_1) + \nu(Re_3F_1) - \nu(Re_1F_2) - \nu(Re_2F_2)]$	$\nu_{13}(E)$	464(<1)[239]
510(2)	516(1)[1]	$\nu_3(A_1)$	$[\nu(Re_1O_D) + \nu(Re_2O_D) + \nu(Re_3O_D)] + [\nu(Re_1F_1) + \nu(Re_3F_1) + \nu(Re_2F_3) + \nu(Re_3F_3) + \nu(Re_1F_2) + \nu(Re_2F_2)]$		
			$[\nu(Re_1F_4) + \nu(Re_2F_4) + \nu(Re_3F_4)] + [\nu(Re_1F_1) + \nu(Re_3F_1) + \nu(Re_2F_3) + \nu(Re_3F_3) + \nu(Re_1F_2) + \nu(Re_2F_2)]$	$\nu_3(A_1)$	438(1)[7]
	407(1)[59]	$\nu_{14}(E)$	$[\nu(Re_1F_1) + \nu(Re_2F_3)] - [\nu(Re_3F_1) + \nu(Re_3F_3)]$		
395 sh[g] 392(7)[g]	401(2)[27]	$\nu_4(A_1)$	$\delta(O_ARe_1O_C) + \delta(O_ARe_2O_C) + \delta(O_ARe_3O_C)$	$\nu_4(A_1)$	403(5)[8]
			$\delta(O_ARe_1O_C) + \rho_w(Re_1O_B) + \delta(O_ARe_1O_C) + \rho_w(Re_1O_B) + \delta(O_ARe_3O_B) + \rho_w(Re_3O_C)$	$\nu_{14}(E)$	396(5)[1]
387(4)[g]	388(1)[50]	$\nu_{15}(E)$	$\delta(O_ARe_2O_C) - \delta(O_ARe_3O_C)$	$\nu_{15}(E)$	391(<0.1)[14]
374(17)	384(5)[1]	$\nu_5(A_1)$	$\delta(O_AO_CRe_1O_B) + \delta(O_AO_CRe_2O_B) + \delta(O_AO_CRe_3O_B)$	$\nu_5(A_1)$	380(2)[1]
368 sh	380(1)[1]	$\nu_{16}(E)$	$\delta(O_CRe_2O_B) + \delta(O_CRe_3O_B) - \delta(O_AO_CRe_1O_B)$	$\nu_{16}(E)$	375(<0.01)[11]
	379(3)[82]	$\nu_{17}(E)$	$\delta(O_CRe_1O_B) + \delta(O_CRe_3O_B) - \delta(O_AO_CRe_2O_B)$	$\nu_{17}(E)$	365(2)[8]
	367(<1)[33]	$\nu_6(A_1)$	$\rho_w(O_ARe_1O_C) + \rho_w(O_ARe_2O_C) + \rho_w(O_ARe_3O_C)$	$\nu_6(A_1)$	351(<1)[25]
345(7)	332(3)[11]	$\nu_{18}(E)$	$[\delta(O_ARe_1O_B) - \delta(O_BRe_1O_C) - \delta(O_ARe_3O_B) + \delta(O_BRe_2O_C) - \delta(O_BRe_2O_C)] + [\nu(Re_1F_3) + \nu(Re_3F_3) - \nu(Re_2F_2) - \nu(Re_3F_2)]$	$\nu_{18}(E)$	275(2)[67]
262 sh	251(1)[12]	$\nu_{19}(E)$	$\rho_r(O_ARe_1O_C) + \rho_r(O_ARe_2O_C) + \rho_r(Re_3O_B) + [\nu(Re_1F_2) + \nu(Re_2F_2)] - [\nu(Re_2F_3) + \nu(Re_3F_3)]$		
257(3)	248(2)[<1]	$\nu_7(A_1)$	$[\nu(Re_1F_2) + \nu(Re_2F_2)] + [\nu(Re_2F_3) + \nu(Re_3F_3)] + [\nu(Re_3F_1) + \nu(Re_1F_1)]$	$\nu_{19}(E)$	252(<1)[3]
			$[\nu(Re_1F_2) + \nu(Re_2F_2)] + [\nu(Re_2F_3) + \nu(Re_3F_3)] + [\nu(Re_3F_1) + \nu(Re_1F_1)] - [\nu(Re_1F_4) + \nu(Re_2F_4) + \nu(Re_3F_4)]$	$\nu_7(A_1)$	286(<1)[12]
197(4) 191(9)	190(2)[<1]	$\nu_8(A_1)$	$\rho_w(Re_1O_B) + \rho_w(Re_2O_B) + \rho_r(Re_3O_B)$	$\nu_8(A_1)$	175(2)[1]
188(8)	182(2)[<0.1]	$\nu_{20}(E)$	$\rho_r(O_ARe_1O_B) + \rho_r(O_AO_BRe_2O_C) + \rho_r(O_AO_BRe_3O_C)$	$\nu_{20}(E)$	173(1)[<1]
	153(2)[<0.1]	$\nu_9(A_1)$	$\rho_r(O_AO_BRe_1O_C) + \rho_r(O_AO_BRe_2O_C) + \rho_r(O_AO_BRe_3O_C)$	$\nu_9(A_1)$	119(1)[<0.001]
	118(<1)[<0.1]	$\nu_{21}(E)$	$\rho_r(O_AO_BRe_1O_C) - \rho_r(O_AO_BRe_3O_C)$	$\nu_{21}(E)$	97(1)[<0.1]
	95(<1)[<1]	$\nu_{22}(E)$	deformation modes	$\nu_{22}(E)$	96(<1)[<1]
	80(<1)[<0.1]	$\nu_{23}(E)$		$\nu_{23}(E)$	44(<1)[<1]

[a]Frequencies are given in cm^{-1}. [b]Values in parentheses denote relative Raman intensities. The Raman spectrum was recorded in an FEP sample tube at −150 °C using 1064-nm excitation. The $[N(CH_3)_4]^+$ cation modes were observed at $\nu_8(E)$, 377(1); $\nu_{19}(T_2)$, 463(5), 460(5), 455(5); $\nu_3(A_1)$, 750(3), 757(12); $\nu_{18}(T_2)$, 949(8), 943(1); $\nu_7(E)$, 1174(1), 1182(2); $\nu_{17}(T_2)$, 1285(1), 1288(2); $\nu_{16}(T_2)$, 1407(5), 1401(3); $\nu_2(A_1)$, $\nu_6(E)$, 1461(9), 1467(8), 2830(2), 2979(9), 2983(9), 2993(8), 3010(7), 3014(7), 3039(17), 3047(10); many combination bands were also observed. The CH_3CN modes were observed at 2938(33), 2737(2), 2294(24), 1457(6), 1454(4), 921(12), 394(5), 392(7). [c]The abbreviations denote a shoulder (sh), broad (br), stretch (ν), bend (δ), rocking (ρ_r), and wag (ρ_w). [d]Values in parentheses denote calculated Raman intensities ($Å^4\ u^{-1}$). Values in square brackets denote calculated infrared intensities ($km\ mol^{-1}$). The B3LYP/aug-cc-pVTZ(-PP) method was used. [e]Band overlapping with a $[ReO_4]^-$ anion band. [f]Band overlapping with a $[N(CH_3)_4]^+$ cation band. [g]Band overlapping with a CH_3CN band. [h]For the atom labeling scheme, see Figure 3.

trend $\nu_{in\text{-}phase}(Re{-}O) > \nu_{out\text{-}of\text{-}phase}(Re{-}O)$, although, as observed for $[ReO_4]^-$ (Table S1), the calculated frequencies appear 30−40 cm^{-1} higher than the experimental values (exptl, 911−978 cm^{-1}; calcd, 942−1018 cm^{-1}). The $\nu_{in\text{-}phase}(Re{-}O)$ and $\nu_{out\text{-}of\text{-}phase}(Re{-}O)$ frequencies are comparable to those observed for $[N(CH_3)_4][ReO_2F_4]$ (972 and 939 cm^{-1}, respectively).[7] The terminal $\nu_{in\text{-}phase}(Re{-}O)$ stretching mode (971/978 cm^{-1}) is shifted to lower frequency when compared with the corresponding modes in $(ReO_3F)_\infty$ (996 cm^{-1}), and $(ReO_2F_3)_\infty$ (1025 cm^{-1}),[7] in accordance with the enhanced negative charge on oxygen that arises from the net −2 charge of the anion, resulting in somewhat weaker Re−O double bonds.

The factor-group split bands at 575/580/586 cm^{-1} correspond to a mode resulting from asymmetric coupling of $\nu(Re{-}O_{\mu 3})$ and $\nu(Re{-}F_\mu)$, in agreement with the calculated frequency (558 cm^{-1}). The symmetrically coupled $\nu(Re{-}O_{\mu 3})$ and $\nu(Re{-}F_\mu)$ mode is assigned to a weak band at 510 cm^{-1} which quantum-chemical calculations predict to occur as a weak

dx.doi.org/10.1021/ic302221y | Inorg. Chem. 2013, 52, 6806−6819

band at 516 cm^{-1} (see Computational Results). The coupled $\nu(Re{-}O_{\mu 3})$ and $\nu(Re{-}F_{\mu})$ stretching modes are comparable to the coupled $\nu(Re{-}F_t)$ and $\nu(Re{-}F_{\mu})$ stretching modes in $[(ReO_2F_3)_2(\mu\text{-}F)]^-$ (554 cm^{-1})[7] and $[(ReO_2F_2)(\mu\text{-}F)_2(ReO_2F_3)_2]^-$ (568 cm^{-1}).[7] Raman bands occurring between 188 and 395 cm^{-1} are assigned to deformation modes, in accordance with the calculated frequencies (182−401 cm^{-1}).

Computational Results. (a) Calculated Structures of $[\{MO_3(\mu\text{-}F)\}_3(\mu_3\text{-}O)]^{2-}$ and $[\{MO_3(\mu\text{-}F)\}_3(\mu_3\text{-}F)]^-$ (M = Re, Tc). The geometries of the $[\{MO_3(\mu\text{-}F)\}_3(\mu_3\text{-}O)]^{2-}$ and $[\{MO_3(\mu\text{-}F)\}_3(\mu_3\text{-}F)]^-$ anions (M = Re, Tc) (Figures 6 and S5, Supporting Information) were optimized under C_{3v} symmetry at the B3LYP/aug-cc-pVTZ(-PP) level of theory and resulted in stationary points with all frequencies real (Tables 5 and S4, Supporting Information). The starting geometries for $[\{MO_3(\mu\text{-}F)\}_3(\mu_3\text{-}O)]^{2-}$ and $[\{MO_3(\mu\text{-}F)\}_3(\mu_3\text{-}F)]^-$ were the crystallographic geometries of the $[\{ReO_3(\mu\text{-}F)\}_3(\mu_3\text{-}O)]^{2-}$ and $[\{TcO_3(\mu\text{-}F)\}_3(\mu_3\text{-}F)]^-$ anions in their respective $[N(CH_3)_4]^+$ (see X-ray Crystallography) and K^+ [13] salts.

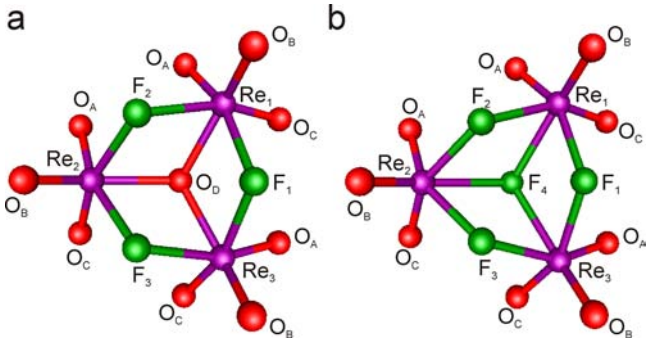

Figure 6. Calculated structures of the (a) $[\{ReO_3(\mu\text{-}F)\}_3(\mu_3\text{-}O)]^{2-}$ and (b) $[\{ReO_3(\mu\text{-}F)\}_3(\mu_3\text{-}F)]^-$ anions (B3LYP/aug-cc-pVTZ(-PP)).

(i) $[\{ReO_3(\mu\text{-}F)\}_3(\mu_3\text{-}O)]^{2-}$. Overall, there is very good agreement between the calculated and experimental Re−O bond lengths and angles (Table 4). Among the experimental trends in geometrical parameters that are reproduced by the calculations are the following: (a) bond lengths; $Re{-}F_{\mu} > Re{-}O_{\mu} > Re{-}O_t$ and (b) bond angles; $O_t{-}Re{-}O_t > O_t{-}Re{-}F_{\mu} > F_{\mu}{-}Re{-}F_{\mu} > F_{\mu}{-}Re{-}O_{\mu 3}$.

(ii) $[\{ReO_3(\mu\text{-}F)\}_3(\mu_3\text{-}F)]^-$. Calculated Geometry of $[\{ReO_3(\mu\text{-}F)\}_3(\mu_3\text{-}F)]^-$ and Comparison with that of $[\{ReO_3(\mu\text{-}F)\}_3(\mu_3\text{-}O)]^{2-}$. The calculated $Re{-}O_t$ bond lengths in the $[\{ReO_3(\mu\text{-}F)\}_3(\mu_3\text{-}F)]^-$ anion are equal to or slightly shorter than those calculated for the $[\{ReO_3(\mu\text{-}F)\}_3(\mu_3\text{-}O)]^{2-}$ anion (Table 4). The $Re{-}O_t$ bonds are equal, whether or not they are trans to $Re{-}F_{\mu 3}$ or $Re{-}F_{\mu}$ bonds, whereas the $Re{-}F_{\mu}$ bond lengths in $[\{ReO_3(\mu\text{-}F)\}_3(\mu_3\text{-}F)]^-$ are significantly shorter than in $[\{ReO_3(\mu\text{-}F)\}_3(\mu_3\text{-}O)]^{2-}$ due to the lower negative charge of the $[\{ReO_3(\mu\text{-}F)\}_3(\mu_3\text{-}F)]^-$ anion relative to that of $[\{ReO_3(\mu\text{-}F)\}_3(\mu_3\text{-}O)]^{2-}$. The $Re{-}F_{\mu 3}$ bond lengths of $[\{ReO_3(\mu\text{-}F)\}_3(\mu_3\text{-}F)]^-$ are significantly longer than the $Re{-}O_{\mu 3}$ bond lengths of $[\{ReO_3(\mu\text{-}F)\}_3(\mu_3\text{-}O)]^{2-}$ because of the greater polarity of the $Re{-}F_{\mu 3}$ bond relative to that of $Re{-}O_{\mu 3}$. The calculated bond length trend for $[\{ReO_3(\mu\text{-}F)\}_3(\mu_3\text{-}F)]^-$, i.e., $Re{-}F_{\mu 3} > Re{-}F_{\mu} > Re{-}O_t$, where all $Re{-}O_t$ bonds are equal, is the same as that observed in the X-ray crystal structure of $[\{TcO_3(\mu\text{-}F)\}_3(\mu_3\text{-}F)]^-$.[13]

All $O_t{-}Re{-}O_t$ angles are essentially equal for both rhenium anions. The $O_t{-}Re{-}F_{\mu}$ angles (where each O_t is trans to F_{μ}) in $[\{ReO_3(\mu\text{-}F)\}_3(\mu_3\text{-}F)]^-$ are smaller than the corresponding $O_t{-}Re{-}O_{\mu}$ angles in $[\{ReO_3(\mu\text{-}F)\}_3(\mu_3\text{-}O)]^{2-}$. The $O_t{-}Re{-}F_{\mu 3}$ angles $[\{ReO_3(\mu\text{-}F)\}_3(\mu_3\text{-}F)]^-$ are larger than the related $O_t{-}Re{-}O_{\mu 3}$ angle (where O_t is trans to $O_{\mu 3}$) in $[\{ReO_3(\mu\text{-}F)\}_3(\mu_3\text{-}O)]^{2-}$. The $Re{-}F_{\mu}{-}Re$ bond angles in $[\{ReO_3(\mu\text{-}F)\}_3(\mu_3\text{-}F)]^-$ are significantly larger than the Re−

Table 6. NBO Natural Charges, Natural Bond Orders, and Valencies for the $[\{MO_3(\mu\text{-}F)\}_3(\mu_3\text{-}O)]^{2-}$ and $[\{MO_3(\mu\text{-}F)\}_3(\mu_3\text{-}F)]^-$ (M = Re, Tc) Anions[a]

	$[\{ReO_3(\mu\text{-}F)\}_3(\mu_3\text{-}O)]^{2-}$		$[\{ReO_3(\mu\text{-}F)\}_3(\mu_3\text{-}F)]^-$		$[\{TcO_3(\mu\text{-}F)\}_3(\mu_3\text{-}O)]^{2-}$		$[\{TcO_3(\mu\text{-}F)\}_3(\mu_3\text{-}F)]^-$	
atom	charges	valencies	charges	valencies	charges	valencies	charges	valencies
$M_{1,2,3}$	2.13	3.93	2.16	3.78	1.82	3.73	1.82	3.63
$F_{1,2,3}$	−0.62	0.55	−0.60	0.61	−0.61	0.58	−0.59	0.61
O_A	−0.60	1.02	−0.57	1.02	−0.49	1.03	−0.44	1.02
O_B	−0.64	1.00	−0.54	1.04	−0.57	1.00	−0.46	1.02
O_C	−0.60	1.02	−0.57	1.02	−0.49	1.03	−0.44	1.02
O_D/F_4	−0.99	1.34	−0.65	0.62	−0.95	0.99	−0.64	0.62
bond		bond order		bond order		bond order		bond order
$M_1{-}O_{A,C}$		0.98		0.98		0.96		0.96
$M_1{-}O_B$		0.96		0.99		0.93		0.95
$M_2{-}O_{A,C}$		0.98		0.98		0.96		0.96
$M_2{-}O_B$		0.96		0.99		0.93		0.95
$M_3{-}O_{A,C}$		0.98		0.98		0.96		0.96
$M_3{-}O_B$		0.96		0.99		0.93		0.95
$M_1{-}O_D/F_4$		0.42		0.20		0.31		0.19
$M_2{-}O_D/F_4$		0.42		0.20		0.31		0.19
$M_3{-}O_D/F_4$		0.42		0.20		0.31		0.19
$M_1{-}F_{1,2}$		0.28		0.30		0.28		0.28
$M_2{-}F_{2,3}$		0.28		0.30		0.28		0.28
$M_3{-}F_{1,3}$		0.28		0.30		0.28		0.28

[a] B3LYP/aug-cc-pVTZ(-PP), (C_{3v}).

dx.doi.org/10.1021/ic302221y | Inorg. Chem. 2013, 52, 6806−6819

F_μ–Re bond angles in $[\{ReO_3(\mu\text{-}F)\}_3(\mu_3\text{-}O)]^{2-}$, whereas the Re–$F_{\mu 3}$–Re angles are smaller than the Re–$O_{\mu 3}$–Re angle.

(iii) $[\{ReO_3(\mu\text{-}F)\}_3(\mu_3\text{-}F)]^-$. Calculated Vibrational Spectrum of $[\{ReO_3(\mu\text{-}F)\}_3(\mu_3\text{-}F)]^-$ and Comparison with That of $[\{ReO_3(\mu\text{-}F)\}_3(\mu_3\text{-}O)]^{2-}$. The $[\{ReO_3(\mu\text{-}F)\}_3(\mu_3\text{-}F)]^-$ anion possesses 42 fundamental vibrational modes belonging to the irreducible representations $9A_1 + 5A_2 + 14E$ under C_{3v} symmetry, where the A_1 and E modes are Raman and infrared active and the A_2 modes are inactive.

The calculated ν(Re–O_t) stretches of $[\{ReO_3(\mu\text{-}F)\}_3(\mu_3\text{-}F)]^-$ (985–1048 cm^{-1}) are expected to appear at higher frequencies (30–43 cm^{-1}) than the calculated ν(Re–O_t) stretches of the $[\{ReO_3(\mu\text{-}F)\}_3(\mu_3\text{-}O)]^{2-}$ anion (Table 5). This is attributed to less electron density donation into the rhenium $d_{t_{2g}}$ orbitals by $F_{\mu 3}$ than by $O_{\mu 3}$. In addition, the higher negative charge of $[\{ReO_3(\mu\text{-}F)\}_3(\mu_3\text{-}O)]^{2-}$ also contributes to enhancement of the Re–O_t bond polarities in $[\{ReO_3(\mu\text{-}F)\}_3(\mu_3\text{-}O)]^{2-}$ and lowering of the O_3Re-group stretching frequencies. Although it is possible to distinguish the two anions based on their ν(Re–O_t) stretching frequencies, the major spectral differences arise from stretching modes involving the triply bridged central atom. In both cases, the ν(Re–F_μ) stretches are predicted to be in-phase and out-of-phase coupled to ν(Re–$X_{\mu 3}$) (X = O; 516 and 558 cm^{-1}, respectively and X = F; 438 and 464 cm^{-1}, respectively). The modes in $[\{ReO_3(\mu\text{-}F)\}_3(\mu_3\text{-}F)]^-$ are not only predicted to occur ca. 100 cm^{-1} lower than in $[\{ReO_3(\mu\text{-}F)\}_3(\mu_3\text{-}O)]^{2-}$, their band intensities are also predicted to be extremely weak. In the experimental spectrum, four bands are observed at 510, 575, 580, and 586 cm^{-1}, and no bands are observed between 400 and 500 cm^{-1}, confirming that the experimental spectrum is that of $[\{ReO_3(\mu\text{-}F)\}_3(\mu_3\text{-}O)]^{2-}$, in accord with the X-ray crystal structure. The deformation mode frequencies are similar in both anions.

(iv) $[\{TcO_3(\mu\text{-}F)\}_3(\mu_3\text{-}O)]^{2-}$ and $[\{TcO_3(\mu\text{-}F)\}_3(\mu_3\text{-}F)]^-$. There is overall good agreement between the calculated and the experimental[13] Tc–O and Tc–F bond lengths of the $[\{TcO_3(\mu\text{-}F)\}_3(\mu_3\text{-}F)]^-$ anion (Table S5). All bond length and bond angle trends of $[\{TcO_3(\mu\text{-}F)\}_3(\mu_3\text{-}O)]^{2-}$ and $[\{TcO_3(\mu\text{-}F)\}_3(\mu_3\text{-}F)]^-$ follow those calculated for their rhenium analogues. The bond angles of both isomers are essentially identical.

(b) Natural Bond Orbital (NBO) Analyses. The bonding in the $[\{MO_3(\mu\text{-}F)\}_3(\mu_3\text{-}O)]^{2-}$ and $[\{MO_3(\mu\text{-}F)\}_3(\mu_3\text{-}F)]^-$ anions (M = Re, Tc) was examined by NBO analyses using the B3LYP/aug-cc-pVTZ(-PP) substitute. The respective NPA charges, valencies, and bond orders (Table 6) are in accordance with anticipated trends: (a) the positive charges are located on the metal atoms (Re, 2.13/2.16; Tc, 1.82/1.82), (b) the three terminal oxygen atoms are doubly bonded (O_t valence, ca. 1.0) to the metal atom (valencies: Re, 3.93/3.78; Tc, 3.73/3.63), (c) the dicoordinate bridging fluorine atoms (F_μ valence: Re, 0.55/0.61; Tc, 0.58/0.61) are equivalently bonded to two metal centers (M–F_μ bond order, ca. 0.3).

Significant differences are found for $O_{\mu 3}$ and $F_{\mu 3}$ bridge-head atoms. For the $[\{MO_3(\mu\text{-}F)\}_3(\mu_3\text{-}O)]^{2-}$ anions, the highest negative charge occurs on $O_{\mu 3}$ (Re, −0.99; Tc, −0.95). The $O_{\mu 3}$ valencies (Re, 1.34; Tc, 0.99) and the M–$O_{\mu 3}$ bond orders (Re, 0.42; Tc, 0.31) of $[\{MO_3(\mu\text{-}F)\}_3(\mu_3\text{-}O)]^{2-}$ show that $O_{\mu 3}$ is equivalently bonded to the three M atoms. The highest negative charges in the $[\{MO_3(\mu\text{-}F)\}_3(\mu_3\text{-}F)]^-$ anions are also located on the bridge-head atom, here $F_{\mu 3}$ (Re, −0.65; Tc, −0.64) and are significantly lower than the $O_{\mu 3}$ charges in the $[\{MO_3(\mu\text{-}F)\}_3(\mu_3\text{-}O)]^{2-}$ anions. The $F_{\mu 3}$ valencies are only slightly higher (Re and Tc, 0.62) than those of the F_μ atoms (valencies: Re and Tc, 0.61; M–F_μ bond orders: Re, 0.30; Tc, 0.28) and are equally shared among the three metal centers (M–$F_{\mu 3}$ bond orders: Re, 0.20; Tc, 0.19).

CONCLUSION

The solvolysis of Re_2O_7 in aHF in the presence of F_2 gas has provided a facile, high-yield, and high-purity synthesis of $(ReO_3F)_\infty$ which has enabled further investigation of its Lewis acid and fluoride ion acceptor properties. The complex resulting from coordination of HF to the metal center, $(HF)_2ReO_3F{\cdot}HF$, was characterized by Raman spectroscopy and single-crystal X-ray diffraction. The study of the fluoride-ion acceptor properties of $(ReO_3F)_\infty$ in CH_3CN has led to the isolation of the novel $[\{ReO_3(\mu\text{-}F)\}_3(\mu_3\text{-}O)]^{2-}$ anion as its $[N(CH_3)_4]^+$ salt, and its characterization in the solid state by Raman spectroscopy and single-crystal X-ray diffraction. The $[\{ReO_3(\mu\text{-}F)\}_3(\mu_3\text{-}O)]^{2-}$ anion was also observed in CH_3CN solvent by ^{19}F NMR spectroscopy. The $[\{ReO_3(\mu\text{-}F)\}_3(\mu_3\text{-}O)]^{2-}$ anion provides the only example of a rhenium oxide fluoride species containing a triply coordinated oxygen atom. Quantum-chemical calculations have been used to model the $[\{ReO_3(\mu\text{-}F)\}_3(\mu_3\text{-}O)]^{2-}$ anion and have provided an energy-minimized geometry that is in very good agreement with the experimental structure. The Raman spectrum of the salt has been fully assigned based on the calculated vibrational modes. The proposed reaction pathways are consistent with the formation of the $[\{ReO_3(\mu\text{-}F)\}_3(\mu_3\text{-}O)]^{2-}$ anion in the basic solvent medium, CH_3CN. Attempts to synthesize the $[N(CH_3)_4]^+$ salt of $[\{ReO_3(\mu\text{-}F)\}_3(\mu_3\text{-}F)]^-$ by analogy with the known technetium analogue failed in CH_3CN and aHF solvents. Quantum-chemical calculations for the known $[\{ReO_3(\mu\text{-}F)\}_3(\mu_3\text{-}O)]^{2-}$ and $[\{TcO_3(\mu\text{-}F)\}_3(\mu_3\text{-}F)]^-$ anions are in very good agreement with their experimental geometries. Quantum-chemical calculations also show that the related, but unknown, $[\{ReO_3(\mu\text{-}F)\}_3(\mu_3\text{-}F)]^-$ and $[\{TcO_3(\mu\text{-}F)\}_3(\mu_3\text{-}O)]^{2-}$ anions are expected to be stable in the gas phase.

EXPERIMENTAL SECTION

Apparatus and Materials. Manipulations involving air-sensitive materials were carried out under anhydrous conditions on glass and metal high-vacuum lines and inside an inert atmosphere drybox as previously described.[39] All preparative work was carried out in vessels constructed from $^1/_4$-in. o.d. lengths of FEP fluoroplastic tubing. The tubing was heat-sealed at one end, heat flared, and connected through a 45° SAE flare nut to the conical end of a Kel-F valve to form a compression seal. Reaction vessels were dried on a Pyrex glass vacuum line and then transferred to a metal vacuum line where they were passivated with ca. 1000 Torr of F_2 for several hours, refilled with dry N_2, and stored in a drybox until used. All vacuum line connections were made by use of $^1/_4$-in. 316 stainless steel Swagelok Ultratorr unions fitted with Viton O-rings.

Acetonitrile (Caledon, HPLC grade) was purified by the literature method[40] and transferred under static vacuum on a glass vacuum line. Anhydrous HF (Harshaw Chemicals Co.) was purified by the literature method.[41] The naked fluoride ion source, $[N(CH_3)_4]F$, was prepared according to the literature method[42] and was stored in an FEP tube in a drybox until used.

Dirhenium heptoxide was prepared by combustion of rhenium powder (Cleveland Refractory Metals, 325 mesh) in a 15-mm o.d. quartz reaction tube. The metal powder (2.178 g, 11.70 mmol) was added to the bottom of the reaction tube. The top of the tube was equipped with a 6-mm J. Young glass valve equipped with a Teflon

dx.doi.org/10.1021/ic302221y | Inorg. Chem. 2013, 52, 6806–6819

barrel. Reduction of the metal powder surface was achieved by heating rhenium powder with a natural gas-oxygen torch in the presence of successive aliquots of H_2 (800−1000 Torr) followed by removal of H_2O under vacuum while the quartz vessel was still hot. The reduction was repeated until water evolution ceased (no condensation was visible on the vessel walls when the reactor was cooled to room temperature). The metal powder was then reduced with two further aliquots of H_2 and flamed dried under dynamic vacuum. The metal powder was then quantitatively converted to Re_2O_7 by addition of successive aliquots of high-purity oxygen gas (Air Liquide, 99.995%), which had been further dried by passing it through a copper coil immersed in dry ice. The metal was heated to a dull red to yellow color with a natural gas-oxygen torch until combustion ceased. Dirhenium heptoxide condensed in the vessel as a bright yellow crystalline material in the cooler regions of the reactor. The procedure was repeated until all the metal was converted to Re_2O_7. After complete combustion, the vessel was evacuated and Re_2O_7 was melted and purified by static vacuum distillation into a 8-mm outer diameter quartz side arm attached to the reaction vessel and was heat-sealed off under ca. 500 Torr of dry N_2. The powdered solid was stored in a drybox until used.

Synthesis of $(ReO_3F)_\infty$. Inside a drybox, Re_2O_7 (0.1399 g, 0.2887 mmol) was weighed into a $^1/_4$-in. o.d. FEP reactor equipped with a Kel-F valve. Anhydrous HF (ca. 2 mL) was condensed onto the solid at −196 °C. The solvolysis reaction was allowed to proceed at room temperature, giving a yellow solution. Three aliquots of F_2 (ca. 1050 Torr each) were added to the reactor at 24 h intervals over 72 h at −78 °C followed by warming to room temperature. Anhydrous HF solvent was removed under dynamic vacuum at −78 °C. The resulting solid complex, $(HF)_2ReO_3F{\cdot}HF$, was further pumped in stages at −40, −20, 0 °C, and room temperature to remove weakly associated and coordinated HF. Further pumping at 50 °C ensured complete removal of HF and resulted in a pale yellow, friable solid. The Raman spectrum of the product was in excellent agreement with the previously published spectrum of $(ReO_3F)_\infty$.[8]

Synthesis of $(HF)_2ReO_3F{\cdot}HF$. Inside a drybox, $(ReO_3F)_\infty$ (0.0587 g, 0.2318 mmol) was weighed into a $^1/_4$-in. o.d. FEP reactor equipped with a side arm and a Kel-F valve. Anhydrous HF (ca. 1 mL) was condensed onto $(ReO_3F)_\infty$ at −196 °C. Upon warming the reaction mixture to room temperature, the solid rapidly dissolved, yielding a yellow solution. The solution was cooled to −78 °C, resulting in the deposition of a crystalline white solid. Raman spectra were recorded for the crystalline solid that deposited at −78 °C under frozen aHF and for the solid that was subsequently isolated by removal of aHF under dynamic vacuum at −78 °C. Both spectra were identical and confirmed the formation of $(HF)_2ReO_3F{\cdot}HF$.

The $(HF)_2ReO_3F{\cdot}HF$ complex was also obtained in solution from three separate room-temperature aHF (ca. 1 mL) solvolysis reactions of $[NH_4][ReO_4]$ (0.0996 g, 0.3713 mmol), $K[ReO_4]$ (0.1343 g, 0.4641 mmol), and Re_2O_7 (0.1071 g, 0.2211 mmol). The solutions were subsequently cooled to −78 °C, which resulted in the deposition of the crystalline white solids. The Raman spectra of these solids under frozen aHF at −150 °C and unit cell determinations of the single crystals confirmed the formation of $(HF)_2ReO_3F{\cdot}HF$.

Synthesis of $[N(CH_3)_4]_2[\{ReO_3(\mu\text{-}F)\}_3(\mu_3\text{-}O)]$. Inside a drybox, $(ReO_3F)_\infty$ (0.0484 g, 0.1912 mmol) and $[N(CH_3)_4]F$ (0.0182 g, 0.1958 mmol) were weighed into a $^1/_4$-in. o.d. FEP reactor at room temperature. The solids were removed from the drybox and cooled to and maintained at −78 °C until dry CH_3CN was condensed onto the solids at −196 °C. A white solid commenced to form upon warming the sample to −40 °C. The reactor was slowly warmed to −20 °C, at which temperature the solid became light beige in color. The solid had partial solubility at −10 °C; however, complete dissolution was only attained at room temperature. Acetonitrile was removed under dynamic vacuum at −40 °C, and the product was completely dried by further pumping at room temperature. The low-temperature Raman spectrum of the dried product corresponded to a mixture of $[N(CH_3)_4]_2[\{ReO_3(\mu\text{-}F)\}_3(\mu_3\text{-}O)]{\cdot}CH_3CN$, $[N(CH_3)_4][ReO_4]$, and $[N(CH_3)_4][ReO_2F_4]$.[7]

Attempted Synthesis of $[N(CH_3)_4][\{ReO_3(\mu\text{-}F)\}_3(\mu_3\text{-}F)]$ from $(ReO_3F)_\infty$ and $[N(CH_3)_4]F$ in CH_3CN Solvent. Inside a drybox, $(ReO_3F)_\infty$ (0.0853 g, 0.3369 mmol) and $[N(CH_3)_4]F$ (0.0110 g, 0.1179 mmol) were weighed into a $^1/_4$-in. o.d. FEP reactor equipped with a side arm and a Kel-F valve. The solid mixture was removed from the drybox and maintained at −78 °C until dry CH_3CN was condensed onto the mixture at −196 °C. A white solid formed upon warming to −35 °C. The reaction mixture was slowly warmed in stages to −20, −10 °C, and room temperature, at which temperature the product showed partial solubility. The low-temperature Raman spectrum of the precipitated product recorded under CH_3CN corresponded to a mixture of $[N(CH_3)_4][ReO_4]$ and $(CH_3CN)_2ReO_3F$.

X-ray Crystallography. (a) Crystal Growth. With the exception of $[N(CH_3)_4][ReO_4]$, crystals were grown in a $^1/_4$-in. o.d. FEP reaction vessel equipped with a side arm (T-shaped reactor) and fitted with a Kel-F valve as previously described.[43] The main arm of the reaction vessel containing the solution was placed inside the precooled glass dewar of the crystal growing apparatus,[43] and the temperature of the dewar and contents was slowly lowered to induce slow crystal growth.

Upon completion of crystal growth, the supernatant was decanted into the side arm, which had been precooled to −196 °C. The crystalline products were dried under dynamic vacuum at the appropriate temperature ($[N(CH_3)_4]_2[\{ReO_3(\mu\text{-}F)\}_3(\mu_3\text{-}O)]{\cdot}CH_3CN$, −5 °C; $[N(CH_3)_4][ReO_4]$, −5 °C; $(HF)_2ReO_3F{\cdot}HF$, −44 °C; and KF·4HF, −78 °C) before the side arm containing the frozen supernatant was heat-sealed off under dynamic vacuum.

(i) $[N(CH_3)_4]_2[\{ReO_3(\mu\text{-}F)\}_3(\mu_3\text{-}O)]{\cdot}CH_3CN$. Crystals of $[N(CH_3)_4]_2[\{ReO_3(\mu\text{-}F)\}_3(\mu_3\text{-}O)]{\cdot}CH_3CN$ were grown from a bright yellow solution obtained by dissolution of 0.0694 g of a reaction mixture containing $[N(CH_3)_4]_2[\{ReO_3(\mu\text{-}F)\}_3(\mu_3\text{-}O)]$, $[N(CH_3)_4][ReO_4]$, and $[N(CH_3)_4][ReO_2F_4]$ (see Syntheses of $(ReO_3F)_\infty$, $(HF)_2ReO_3F$, and $[N(CH_3)_4]_2[\{ReO_3(\mu\text{-}F)\}_3(\mu_3\text{-}O)]$ and Scheme 1) in CH_3CN at room temperature. The solution was prepared in a $^1/_4$-in. o.d. FEP T-shaped reactor followed by pressurization with ca. 1 atm of dry nitrogen. Cooling the solution to −1 °C inside a crystal growing apparatus[43] resulted in the formation of colorless plates over a period of 1.5−2 h. A crystal of $[N(CH_3)_4]_2[\{ReO_3(\mu\text{-}F)\}_3(\mu_3\text{-}O)]{\cdot}CH_3CN$ having the dimensions 0.24 × 0.12 × 0.06 mm^3 was selected for a low-temperature X-ray structure determination.

(ii) $[N(CH_3)_4][ReO_4]$. Crystals of $[N(CH_3)_4][ReO_4]$ were obtained from the product mixture resulting from the reaction of $(ReO_3F)_\infty$ (0.0368 g, 0.1454 mmol) and $[N(CH_3)_4]F$ (0.0273 g, 0.2935 mmol) at −35 °C in CH_3CN in a $^1/_4$-in. o.d. FEP T-shaped reactor (eq 6). The white solid partially dissolved in CH_3CN at room temperature forming a pale yellow solution. The solution was cooled to −3 °C inside a crystal growing apparatus,[43] whereupon colorless blocks formed over a period of 3−4 h. The solution was further cooled to −5 °C for 1 h to ensure more complete crystallization. A crystal of $[N(CH_3)_4][ReO_4]$ having the dimensions 0.15 × 0.30 × 0.31 mm^3 was selected for a low-temperature X-ray structure determination.

(iii) $(HF)_2ReO_3F{\cdot}HF$. Crystals of $(HF)_2ReO_3F{\cdot}HF$ were grown from a pale yellow solution obtained by dissolving $(ReO_3F)_\infty$ (0.0587 g, 0.2318 mmol) in aHF at room temperature. The solution was prepared in a $^1/_4$-in. o.d. FEP T-shaped reactor, which was pressurized with ca. 1 atm of dry nitrogen. The solution was cooled to −36 °C inside a crystal growing apparatus, whereupon colorless plates formed over a period of 4−5 h. A crystal of $(HF)_2ReO_3F{\cdot}HF$ having the dimensions 0.37 × 0.33 × 0.06 mm^3 was selected for a low-temperature X-ray structure determination.

(b) Collection and Reduction of X-ray Data. Crystals were selected at −105 ± 3 °C for low-temperature X-ray structure determination and were mounted in a cold stream (−173 °C) on a goniometer head as previously described.[43] Crystals were centered on a Bruker SMART APEX2 diffractometer, equipped with an APEX2 4K CCD area detector and a triple-axis goniometer, controlled by the APEX2 Graphical User Interface (GUI) software,[44] and a sealed source emitting graphite monochromated Mo−Kα radiation (λ = 0.71073 Å). Diffraction data collection at −173 °C consisted of a full ϕ-rotation at a fixed χ = 54.74° with 0.36° (1010) frames, followed by a series of short (250 frames) ω-scans at various ϕ-settings to fill the

dx.doi.org/10.1021/ic302221y | Inorg. Chem. 2013, 52, 6806−6819

gaps. The crystal-to-detector distances were 4.952, 4.952, 4.955, and 4.953 cm for $[N(CH_3)_4]_2$-$[\{ReO_3(\mu\text{-}F)\}_3(\mu_3\text{-}O)]\cdot CH_3CN$, $[N(CH_3)_4][ReO_4]$, $(HF)_2ReO_3F\cdot HF$, and KF·4HF, respectively, and the data collections were carried out in a 512 × 512 pixel mode using 2 × 2 pixel binning. Processing of the raw data sets were completed by using the APEX2 GUI software,[44] which applied Lorentz and polarization corrections to three-dimensionally integrated diffraction spots. The program, SADABS,[45] was used for the scaling of diffraction data, the application of decay corrections, and empirical absorption corrections based on the intensity ratios of redundant reflections.

(c) Solution and Refinement of the Structures. The XPREP[46] program was used to confirm the unit cell dimensions and the crystal lattices. The solution was obtained by direct methods which located the positions of the Re atoms in the structures of $[N(CH_3)_4]_2$-$[\{ReO_3(\mu\text{-}F)\}_3(\mu_3\text{-}O)]\cdot CH_3CN$, $[N(CH_3)_4][ReO_4]$, and $(HF)_2ReO_3F\cdot HF$ and the K atom in the structure of KF·4HF. The positions of all fluorine and oxygen atoms were revealed in successive difference Fourier syntheses. The hydrogen atoms could not be located in the case of $(HF)_2ReO_3F\cdot HF$ and KF·4HF, but their positions were calculated in the cases of $[N(CH_3)_4]_2$-$[\{ReO_3(\mu\text{-}F)\}_3(\mu_3\text{-}O)]\cdot CH_3CN$, and $[N(CH_3)_4][ReO_4]$. The final refinement was obtained by introducing anisotropic thermal parameters and the recommended weightings for all of the atoms. The maximum electron densities in the final difference Fourier maps were located near the heavy atoms. All calculations were performed using the SHELXTL-plus package[46] for the structure determinations and solution refinements and for the molecular graphics. The choices of space group for $[N(CH_3)_4]_2[\{ReO_3(\mu\text{-}F)\}_3(\mu_3\text{-}O)]\cdot CH_3CN$, $[N(CH_3)_4][ReO_4]$, $(HF)_2ReO_3F\cdot HF$, and KF·4HF were confirmed by Platon from the WinGX software package.[47]

In the case of the $(HF)_2ReO_3F\cdot HF$ structure, the axial oxygen and fluorine atoms are positionally disordered, although not related by symmetry. A similar disorder is observed for the HF molecules. Attempts to resolve the O/F positions into two components were unsuccessful. The possibility of twinning was also explored. In both cases, the H atoms of the HF molecules could not be located in the difference Fourier maps.

Nuclear Magnetic Resonance Spectroscopy. (a) NMR Instrumentation and Spectral Acquisitions. The spectra were acquired on a Bruker Avance II 600 MHz NMR spectrometer, equipped with a TBI-Z probehead and BCU05 temperature unit. The ^{19}F NMR spectra were externally referenced to $CFCl_3$. The ^{19}F NMR spectrum of an equimolar mixture of $[N(CH_3)_4]F$ and $(ReO_3F)_\infty$ in CH_3CN was acquired at 564.686 MHz in a 128 K memory with a spectral width setting of 84746 Hz, yielding an acquisition time of 0.77 s and a data point resolution of 0.64 Hz/data point. The number of transients accumulated was 128; a pulse width of 4.53 μs and a line broadening of 1.0 Hz were used.

(b) NMR Sample Preparation. Samples of product mixtures resulting from the reactions of $(ReO_3F)_\infty$ with $[N(CH_3)_4][ReO_4]$ in CH_3CN (containing the reaction products, $[N(CH_3)_4]_2[\{ReO_3(\mu\text{-}F)\}_3(\mu_3\text{-}O)]\cdot CH_3CN$, $[N(CH_3)_4][ReO_4]$, and $[N(CH_3)_4][ReO_2F_4]$) were prepared in $^1/_4$-in. o.d. FEP reactors as described above. NMR samples were prepared by transfer of the reaction mixture solutions under anhydrous conditions into 4-mm o.d. FEP NMR sample tubes which were then outfitted with Kel-F valves as previously described.[48] The NMR sample tubes were connected to a glass vacuum line through their valve assemblies, cooled to −196 °C, heat-sealed under dynamic vacuum, and stored at −196 °C until NMR spectra could be obtained. Samples were rapidly dissolved at room temperature just prior to data acquisition at 27 °C. When recording the spectra, the 4-mm o.d. FEP tubes were inserted into 5-mm o.d. thin-wall precision glass NMR tubes (Wilmad).

Raman Spectroscopy. Low-temperature (−150 °C) Raman spectra were recorded on a Bruker RFS 100 FT Raman spectrometer using 1064-nm excitation and a resolution of 1 cm^{-1} as previously described.[43] The spectra were recorded using a laser power of 300 mW and a total of 1200 scans for each spectrum.

Computational Details. Calculations were carried out using the Gaussian 03[49] (NBO) or Gaussian 09[50] (geometry optimization and vibrational frequencies) software packages. Geometries were fully optimized using density functional theory (B3LYP) with aug-cc-pVTZ (O and F) and aug-cc-pVTZ-PP (Tc and Re) basis sets. All basis sets were obtained online from the EMSL Basis Set Exchange (https://bse.pnl.gov/bse/portal).[51,52] Fundamental vibrational frequencies were calculated along with Raman intensities, and were obtained for the optimized local minima. The program, GaussView,[53] was used to visualize the vibrational displacements that form the basis of the vibrational mode descriptions and assignments given in this work.

Calculations of NMR chemical shifts were carried out using the Amsterdam Density Functional (ADF) 2010.2 program package[54−56] and the implemented NMR module.[57−61] Single-point energies were obtained for the B3LYP/aug-cc-pVTZ geometries at the PBE0 level of theory utilizing Slater type all electron TZ2P basis sets. Relativistic effects were included with the spin−orbit coupled zeroth-order regular approximation (ZORA) methodology.

The calculated chemical shifts (δ_{calcd}) reported in this work (see NMR Spectroscopy) were obtained according to eq 7

$$\delta_{calcd} = \delta_{ref} + \sigma_{ref} - \sigma_{calcd} \quad (7)$$

where δ_{ref} is the experimental chemical shift (−141.2 ppm)[7] of the reference, μ-F in $[(ReO_2F_3)_2(\mu\text{-}F)]^-$; σ_{ref} is the calculated NMR shielding of the reference nucleus (296.71 ppm); σ_{calcd} is the calculated NMR shielding of the nucleus under study, i.e., $\sigma_{\mu\text{-}F}$ = 334.76 ppm in $[\{ReO_3(\mu\text{-}F)\}_3(\mu_3\text{-}O)]^{2-}$ and $\sigma_{\mu\text{-}F}$ = 351.40 ppm and $\sigma_{\mu 3\text{-}F}$ = 359.35 ppm in $[\{ReO_3(\mu\text{-}F)\}_3(\mu_3\text{-}F)]^-$; giving calculated chemical shifts of $\delta_{\mu\text{-}F}$ = −179.3 ppm for $[\{ReO_3(\mu\text{-}F)\}_3(\mu_3\text{-}O)]^{2-}$ and $\delta_{\mu\text{-}F}$ = −195.9 ppm and $\delta_{\mu 3\text{-}F}$ = −203.9 ppm for $[\{ReO_3(\mu\text{-}F)\}_3(\mu_3\text{-}F)]^-$.

■ ASSOCIATED CONTENT

Ⓢ Supporting Information

Raman spectrum of $(ReO_3F)_\infty$ and calculated geometry for monomeric ReO_3F (C_{3v}) (Figure S1); alternative proposed reaction pathway leading to the formation of the $[\{ReO_3(\mu\text{-}F)\}_3(\mu_3\text{-}O)]^{2-}$ anion (Scheme S1); proposed reaction pathway leading to the formation of the $[\{TcO_3(\mu\text{-}F)\}_3(\mu_3\text{-}F)]^-$ anion (Scheme S2); crystal growth of KF·4HF and X-ray crystal structure of KF·4HF (Figure S2); view of the crystal packing of $[N(CH_3)_4]_2[\{ReO_3(\mu\text{-}F)\}_3(\mu_3\text{-}O)]\cdot CH_3CN$ along the *c*-axis (Figure S3); crystal structure of $[N(CH_3)_4][ReO_4]$ (Figure S4); discussion of the Raman spectrum of $[N(CH_3)_4][ReO_4]$; Vibrational data for the $[ReO_4]^-$ anion (Table S1); correlation diagram for the vibrational modes of $(HF)_2ReO_3F$ (Table S2); correlation diagram for the vibrational modes of the $[\{ReO_3(\mu\text{-}F)\}_3(\mu_3\text{-}O)]^{2-}$ anion (Table S3); calculated structures of the $[\{TcO_3(\mu\text{-}F)\}_3(\mu_3\text{-}O)]^{2-}$ and $[\{TcO_3(\mu\text{-}F)\}_3(\mu_3\text{-}F)]^-$ anions (Figure S5); calculated vibrational data and geometrical parameters for the $[\{TcO_3(\mu\text{-}F)\}_3(\mu_3\text{-}O)]^{2-}$ and $[\{TcO_3(\mu\text{-}F)\}_3(\mu_3\text{-}F)]^-$ anions (Tables S4 and S5); complete references 49, 50, and 56. This information is available free of charge via the Internet at http://pubs.acs.org/.

■ AUTHOR INFORMATION

Corresponding Author

*E-mail: schrobil@mcmaster.ca.

Notes

The authors declare no competing financial interest.

■ ACKNOWLEDGMENTS

We thank the Natural Sciences and Engineering Research Council (NSERC) of Canada for support in the form of a Discovery Grant (G.J.S.), the Ontario Ministry of Training Colleges and Universities and NSERC for support in the form of graduate scholarships (M.I.), the Government of Canada for the award of a postdoctoral fellowship (T.K.), and the

computational resources provided by SHARCNet (Shared Hierarchical Academic Research Computing Network; www.sharcnet.ca).

REFERENCES

(1) Wiechert, K. *Z. Anorg. Allg. Chem.* **1950**, *261*, 310−323.
(2) Kuhlmann, W.; Sawodny, W. *J. Fluorine Chem.* **1977**, *9*, 337−340.
(3) Kuhlmann, W.; Sawodny, W. *J. Fluorine Chem.* **1977**, *9*, 341−357.
(4) Yagodin, G. A.; Opalovskii, A. A.; Rakov, E. G.; Dudin, A. S. *Dokl. Akad. Nauk. SSSR* **1980**, *252*, 1400−1403; *Dokl. Chem.* **1980**, *252*, 316−318.
(5) Gerlach, U.; Ringel, C. *Z. Chem.* **1977**, *17*, 306−307.
(6) Gerken, M.; Dixon, D. A.; Schrobilgen, G. J. *Inorg. Chem.* **2000**, *39*, 4244−4255.
(7) Casteel, W. J., Jr.; Dixon, D. A.; LeBlond, N.; Lock, P. E.; Mercier, H. P. A.; Schrobilgen, G. J. *Inorg. Chem.* **1999**, *38*, 2340−2358.
(8) Supel, J.; Marx, R.; Seppelt, K. *Z. Anorg. Allg. Chem.* **2005**, *631*, 2979−2986.
(9) Engelbrecht, A.; Grosse, A. V. *J. Am. Chem. Soc.* **1954**, *76*, 2042−2045.
(10) Ansley, E. E.; Hair, M. L. *J. Chem. Soc.* **1958**, *76*, 3747−3748.
(11) Sunder, W. A.; Stevie, F. A. *J. Fluorine Chem.* **1975**, *6*, 449−463.
(12) Selig, H.; El-Gad, U. *J. Inorg. Nucl. Chem.* **1973**, *35*, 3517−3522.
(13) Supel, J.; Abram, U.; Hagenbach, A.; Seppelt, K. *Inorg. Chem.* **2007**, *46*, 5591−5595.
(14) Okrasinski, S.; Mitra, G. *J. Inorg. Nucl. Chem.* **1974**, *36*, 1908−1909.
(15) Binenboym, J.; El-Gad, U.; Selig, H. *Inorg. Chem.* **1974**, *13*, 319−321.
(16) Saielli, G.; Bini, R.; Bagno, A. *Theor. Chem. Acc.* **2012**, *131*, 1140 and references therein.
(17) Saielli, G.; Bini, R.; Bagno, A. *Theor. Chem. Acc.* **2012**, *131*, 1283.
(18) Christe, K. O.; Curtis, E. C.; Mercier, H. P.; Sanders, J. C. P.; Schrobilgen, G. J.; Dixon, D. A. *J. Am. Chem. Soc.* **1991**, *113*, 3351−3361.
(19) Casteel, W. J., Jr.; MacLeod, D. M.; Mercier, H. P. A.; Schrobilgen, G. J. *Inorg. Chem.* **1996**, *35*, 7279−7288.
(20) Hughes, M. J.; Gerken, M.; Mercier, H. P. A.; Schrobilgen, G. J. *Inorg. Chem.* **2010**, *49*, 4768−4780.
(21) Krebs, B.; Hasse, K.-D. *Acta Crystallogr.* **1976**, *B32*, 1334−1337.
(22) Kruger, G. J.; Reynhardt, E. C. *Acta Crystallogr.* **1978**, *B34*, 259−261.
(23) Tramšek, M.; Goreshnik, E.; Žemva, B. *J. Fluorine Chem.* **2009**, *130*, 1093−1098.
(24) Gerken, M.; Dixon, D. A.; Schrobilgen, G. J. *Inorg. Chem.* **2002**, *41*, 259−277.
(25) Mercier, H. P. A.; Schrobilgen, G. J. *Inorg. Chem.* **1993**, *32*, 145−151.
(26) von Mattes, R.; Mennemann, K. *Z. Anorg. Allg. Chem.* **1977**, *437*, 175−182.
(27) Cotton, F. A.; Mague, J. T. *Inorg. Chem.* **1964**, *3*, 1402−1407.
(28) Mucker, K.; Smith, G. S.; Johnson, Q. *Acta Crystallogr.* **1968**, *B24*, 874−879.
(29) Watson, W. H., Jr.; Waser, J. *Acta Crystallogr.* **1958**, *11*, 689−692.
(30) Tragl, S.; Ströbele, M.; Glasser, J.; Vicent, C.; Llusar, R.; Meyer, H.-J. *Inorg. Chem.* **2009**, *48*, 3825−3831.
(31) Krebs, B.; Müller, A.; Beyer, H. H. *Inorg. Chem.* **1969**, *8*, 436−443.
(32) Bertolucci, A.; Freni, M.; Romiti, P.; Ciani, G.; Sironi, A.; Albano, V. G. *J. Organomet. Chem.* **1976**, *113*, C61−C64.
(33) Roesky, H. W.; Hesse, D.; Bohra, R.; Noltemeyer, M. *Chem. Ber.* **1991**, *124*, 1913−1915.
(34) Kabisch, G.; Klose, M. *J. Raman Spectrosc.* **1978**, *7*, 311−315.
(35) Kabisch, G. *J. Raman Spectrosc.* **1980**, *9*, 279−285.
(36) Berg, R. W. *Spectrochim. Acta* **1978**, *34A*, 655−659.
(37) Korppi-Tommola, J.; Brown, R. J. C.; Shurvell, H. F.; Sala, O. *J. Raman Spectrosc.* **1981**, *11*, 363−368.
(38) Park, Y. S.; Shurvell, H. F.; Brown, R. J. C. *J. Raman Spectrosc.* **1986**, *17*, 351−354.
(39) Casteel, W. J., Jr.; Dixon, D. A.; Mercier, H. P. A.; Schrobilgen, G. J. *Inorg. Chem.* **1996**, *35*, 4310−4322.
(40) Winfield, J. M. *J. Fluorine Chem.* **1984**, *25*, 91−98.
(41) Emara, A. A. A.; Schrobilgen, G. J. *Inorg. Chem.* **1992**, *31*, 1323−1332.
(42) Christe, K. O.; Wilson, W. W.; Wilson, R. D.; Bau, R.; Feng, J.-A. *J. Am. Chem. Soc.* **1990**, *112*, 7619−7625.
(43) Lehmann, J. F.; Dixon, D. A.; Schrobilgen, G. J. *Inorg. Chem.* **2001**, *40*, 3002−3017.
(44) *APEX2*, release 2.0−2; Bruker AXS Inc.: Madison, WI, 2010.
(45) Sheldrick, G. M. *SADABS (Siemens Area Detector Absorption Corrections)*, version 2.10; Siemens Analytical X-ray Instruments, Inc.: Madison, WI, 2004.
(46) Sheldrick, G. M. *SHELXTL*, release 6.14; Siemens Analytical X-ray Instruments, Inc.: Madison, WI, 2008.
(47) Spek, A. L. *J. Appl. Crystallogr.* **2003**, *36*, 7−13.
(48) Brock, D. S.; Bilir, V.; Mercier, H. P. A.; Schrobilgen, G. J. *J. Am. Chem. Soc.* **2007**, *129*, 3598−3611.
(49) Frisch, M. J.; et al. *Gaussian 03*, revision D.01; Gaussian, Inc.: Wallingford, CT, 2004.
(50) Frisch, M. J.; et al. *Gaussian 09*, revision C.01; Gaussian, Inc.: Wallingford, CT, 2010.
(51) Feller, D. *J. Comput. Chem.* **1996**, *17*, 1571−1586.
(52) Schuchardt, K. L.; Didier, B. T.; Elsethagen, T.; Sun, L.; Gurumoorthi, V.; Chase, J.; Li, J.; Windus, T. L. *J. Chem. Inf. Model.* **2007**, *47*, 1045−1052.
(53) Dennington, R. I.; Keith, T.; Millam, J. M.; Eppinnett, K.; Hovell, W. L.; Gilliland, R. *GaussView*, version 3.07 ed.; Semichem, Inc.: Shawnee Mission, KS, 2003.
(54) te Velde, G.; Bickelhaupt, F. M.; Baerends, E. J.; Fonseca Guerra, C.; van Gisbergen, S. J. A.; Snijders, J. G.; Ziegler, T. *J. Comput. Chem.* **2001**, *22*, 931−967.
(55) Fonseca Guerra, C.; Snijders, J. G.; te Velde, G.; Baerends, E. J. *Theor. Chem. Acc.* **1998**, *99*, 391−403.
(56) Baerends, E. J.; et al. *ADF* 2010, SCM, Theoretical Chemistry; Vrije Universiteit: Amsterdam, The Netherlands, http://www.scm.com.
(57) Krykunov, M.; Ziegler, T.; van Lenthe, E. *Int. J. Quantum Chem.* **2009**, *109*, 1676−1683.
(58) Schreckenbach, G.; Ziegler, T. *J. Phys. Chem.* **1995**, *99*, 606−611.
(59) Schreckenbach, G.; Ziegler, T. *Int. J. Quantum Chem.* **1997**, *61*, 899−918.
(60) Wolff, S. K.; Ziegler, T. *J. Chem. Phys.* **1998**, *109*, 895−905.
(61) Wolff, S. K.; Ziegler, T.; van Lenthe, E.; Baerends, E. J. *J. Chem. Phys.* **1999**, *110*, 7689−7698.